IEEE Access
Multidisciplinary | Rapid Review | Open Access Journal

Received August 20, 2020, accepted September 2, 2020, date of publication September 9, 2020,
date of current version September 25, 2020.

Digital Object Identifier 10.1109/ACCESS.2020.3023036

Research on Electromagnetic Scattering Characteristics of Combined Conducting and Dielectric Target Above Coastal Environment

GAO XIANG ZOU, CHUANGMING TONG, HUA LONG SUN, AND PENG PENG
Air and Missile Defense College, Air Force Engineering University, Xi'an 710051, China

Corresponding author: Gao Xiang Zou (gxiangzou@163.com)

This work was supported by the National Natural Science Foundations of China under Grant 61372033 and Grant 61901510.

ABSTRACT The electromagnetic (EM) scattering characteristics of target above coastal environment are complicated due to the simultaneous existence of ground region and sea region. Nevertheless, the actual target possesses both conducting part and dielectric part. Such a composite scattering problem involves multiple media parameters and large amount of unknowns. Hence, aiming at accurately and efficiently calculating the EM scattering from combined conducting and dielectric target above coastal environment, the hybrid SIE-KA method is introduced in which single integral equation (SIE) method is utilized to reduce the number of combined target's unknowns and Kirchhoff approximation (KA) is applied to obtain induced electric and magnetic current on the surface of coastal environment. Moreover, multilevel fast multipole algorithm (MLFMA) is adopted to significantly reduce the computational cost and memory requirement. Several numerical examples demonstrate the accuracy and efficiency of the hybrid method. Finally, the EM scattering characteristics of combined conducting and dielectric target above coastal environment have been studied. The radar cross section (RCS) curves with different category of environment, polarization mode, working frequency, statistic parameters of coastal environment, permittivity of target's dielectric part, target's height and target category have been analyzed in detail to provide some useful conclusions. The approach and results can be broadly applied in remote sensing simulation of coastal environment with combined target.

INDEX TERMS Coastal environment, electromagnetic scattering, Kirchhoff approximation, single integral equation, multilevel fast multipole algorithm, combined conducting and dielectric target.

I. INTRODUCTION

Recent years have seen the rapid development of metamaterials, plasmonics, metasurface, graphene, AI-based algorithms [1]–[5]. Simultaneously, the theories for analyzing electromagnetic (EM) scattering from target above real environment have attracted many researchers' interests due to numerous applications in radar surveillance, target detection and remote sensing etc., [6]–[9]. Numerical simulation for target above environment is complicated by the complex EM scattering mechanism between target and environmental surface. Thus, the computation algorithms have been extensively studied to solve composite scattering model. The typical computation algorithms can be divided into three major categories: analytical method [10], [11], numerical method [12], [13] and high-frequency asymptotic method [14]. Nevertheless, there are certain disadvantages associated with the application of analytical method: firstly, it is only suitable for handling the symmetrical objects with simple boundary condition, e.g., sphere, cylinder and plane; secondly, it cannot handle several complex media situations, e.g., objects coated with inhomogeneous material, combined conducting and dielectric target or divisional circumstances. On the other hand, numerical methods are widely utilized to analyze the EM scattering characteristics of target and environments. Among them, method of moment (MOM) [15] becomes the representative method due to its great universality and accuracy. Nevertheless, the main drawback of purely MOM is that the high computational complexity and huge memory requirement are unavoidable when handling the scattering

The associate editor coordinating the review of this manuscript and approving it for publication was Bo Pu.

problems with larger unknowns. Many relevant optimization methods have been proposed which mainly focus on two key points: one is to accelerating process of solving matrix equation by manipulating impendence matrix, e.g., multilevel fast multipole algorithm (MLFMA) [16], banded matrix iterative approach/canonical grid method (BMIA/CAG) [17], multilevel sparse matrix canonical grid method (MSMCG) [18], extended propagation-inside-layer expansion (EPILE) [19], or simplifying matrix structure, e.g., integral equation domain decomposition method (IE-DDM) [20], electric/magnetic current combined-field integral equation and domain decomposition method (JMCFIE-DDM) [21]; the other is to reduce the number of unknowns like by introducing the single integral equation (SIE) [22], which remarkably cut off half of unknowns compared with that using the coupled integral equation. Besides these strategies above, some methods depending on computer technology [23], [24] as parallel computing with CPU or GPU have become practicable way to improve the computation efficiency of numerical method. Previous works focused on the analysis of EM scattering from pure conductor or pure dielectric target. The scattering problems of composite target have attracted many researchers' interests due to its practical significance. Fuscaldo *et al.* [25] furnished a convenient analytical framework based on KA for analysis of EM scattering from composite target. Xu *et al.* [26] utilized a synthetic basis functions method (SBFM) to analyze scattering properties of nonperiodic composite metallic and dielectric structures. Cheng *et al.* [27] proposed an time-domain fast dipole method to accelerate the time-domain volume-surface integral equation for calculating the transient EM scattering from composite conducting-dielectric target. Li *et al.* [28] proposed a nonconformal and nonoverlapping DDM based on hybrid volume and surface integral equation (VSIE) to compute the scattering from composite target. However, these works mainly solve the scattering problems of single composite target. When actual environment is taken into consideration with the target, the surface subdivision of rough surface generates a great mass of unknowns, which would lead to unbearable memory requirement. Therefore, aiming at overcoming this problem, the high-frequency asymptotic method is introduced to compute the scattering from the environment part efficiently. The Kirchhoff approximation (KA) [12] is the representative method, which is utilized to obtain the induced electric and magnetic current of rough surface. Some researchers have solved the scattering problem of target with large-scale environment efficiently by hybrid MOM-KA method [29]–[31]. So far, previous scholars have done large quantities of works to explore the EM scattering characteristics of target and environment. Deficiently, actual targets and circumstances are characterized with complex media, which are always simplified or ignored in the research process. Firstly, in terms of target, there are both conducting part and dielectric part existing simultaneously, e.g., stealth aircraft with metallic body and thin dielectric coating, conducting antenna with dielectric radomes, and metal cruise missile equipped with dielectric warhead. Then, in terms of environment, there are diverse regions with different media properties coexisting, e.g., the coastal environment, water zone embedded in land surface, and blocked cultivated land. If such complex conditions are all taken into consideration, the EM scattering problem of target and environment will be more complicated. Previous works mainly focused on the pure land surface or pure sea surface with target. In this paper, the coastal composite rough surface is considered with the combined target, where the composite scattering model is closer to the actual detection situation in coastal environment. The dual-complexity of both combined target and coastal environment makes the EM scattering characteristic be controlled by plenty of factors.

Previous works about divisional environment modeling in our research group have been proposed, e.g., the modeling method for the water zone embedded in land surface [32], ground and near sea in adjacent region [33] and island in deep sea [34]. A borderline modeling method of fractal boundary for divisional environment has been proposed in [35]. The core concept of modeling method for divisional rough surface can be divided into three parts: first, adopting Gaussian spectral function to generate the rough surface for ground region; secondly, selecting suitable sea spectrum to simulate the rough surface for sea region; finally, according to the concrete shape of coastline, choosing suitable weighted inverse tangent function to construct the borderline between two regions. A major advantage of this modeling method is that it can guarantee the statistic property of each region remain invariant and connect two areas smoothly. In [34], Pierson-Moskowitz (PM) sea spectrum was chose for build up the surface of deep sea, but in [33], considering the effect of finite water depth in near sea region, JONSWAP spectral function combined with shallow coefficient was utilized to generate the near sea surface. However, there are certain drawbacks associated with the use of this modeling method. Firstly, this is an approximated theoretical model which lacks the validation of practical experiments due to limited experimental condition of our research group. Secondly, it is just a surface model without considering layered structure. Nevertheless, it provides an attempt to simulate the coastal environments for electromagnetic computation. In this present work, we quote the geometrical model [33] to describe the surface properties of coastal environment. Based on the geometrical model of coastal environment, the combined target is introduced to form the composite scattering model. In [36], we have proposed the methodology to analyze the combined target above single environment. However, the hybrid SIE-KA-FMM method proposed in [36] could just be utilized to solve the combined target with PEC surface. In this paper, coastal environment has diverse media properties, which leads to the coexistence of both induced electric current and induced magnetic current on the facet of coastal composite rough surface. Hence, we propose the new version of hybrid SIE-KA method for combined target above coastal environment, where MLFMA is utilized to

further reduce memory requirement and computation consume. What's more, the combined target with this kind of divisional environment will lead to more complicated scattering mechanism. It is of practical significance to research such scattering problems. The unique phenomena and conclusions found in this paper will provide a good data support for the field of radar detection and remote sensing.

The rest of paper is organized as following: In Section II, we review the notations and formulations of the SIE-KA and provide the new version adjusting to the coastal environment. We then discuss the acceleration of SIE-KA using MLFMA. Several examples verify the validation of SIE-KA-MLFMA. In Section III, EM scattering characteristics of combined conducting and dielectric target above single environment and coastal environment are compared. The influences of polarization mode, working frequency, root mean square (RMS) height and correlation length of ground region, wind velocity of near sea region, permittivity of target's dielectric part, target's height and target category on scattering characteristic are discussed in detail. In Section IV, some conclusions are provided and a proposition for further investigation is given.

II. FORMULATION

A. HYBRID SIE-KA METHOD

In hybrid SIE-KA method, the geometrical configuration utilized to solve the composite scattering problem of the combined conducting and dielectric target above coastal environment is illustrated in Figure 1.

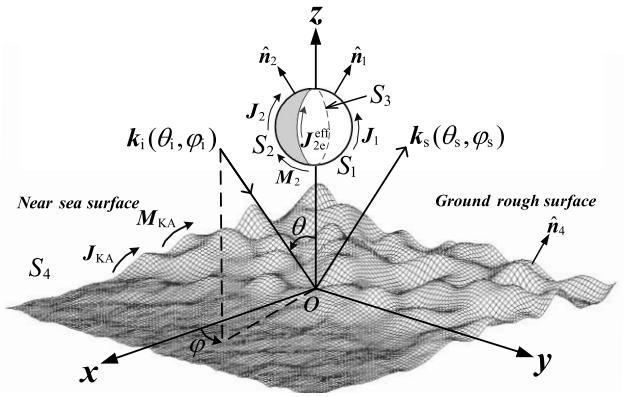

FIGURE 1. Geometry configuration for the EM scattering from a combined conducting and dielectric target above coastal environment.

Both target and environment are disserted by triangulation. With regard to coastal environment surface generation, the modeling method for the divisional rough surface is introduced referring to Ref. [33]. The combined target includes perfect electric conductor (PEC) part and dielectric part, where S_1 and S_2 present their surface respectively. S_3 presents contacting surface between PEC part and dielectric part. S_4 presents the coastal environment. N_1 is the total number of edges in S_1 which includes the common edges of contacting boundary between S_1 and S_2, and N_2 is the total number of edges in S_2 which doesn't include the common edges. N_3 and N_4 present the total number of edges in S_3 and S_4 respectively.

In this paper, a tapered incident beam is introduced in order to circumvent artificial truncation effects. We utilize the 3-D form of tapered incident beam, and the concrete forms are given in the Equation (8) in Ref. [32]. In Figure 1, θ and φ denote pitching angle and azimuth angle, respectively. As described above, when the composite scattering model is illuminated by incident EM wave, there is equivalent electric current or equivalent magnetic current appearing along the surface. On the surface S_1 of PEC part, only equivalent electric current will be stimulated, which is denoted by $\boldsymbol{J}_1$. Moreover, both equivalent electric current and magnetic current will be stimulated along the dielectric surface, which are denoted by $\boldsymbol{J}_2, \boldsymbol{M}_2$ on S_2 and $\boldsymbol{J}_{\mathrm{KA}}, \boldsymbol{M}_{\mathrm{KA}}$ on S_4, respectively. As we already known, the equivalent electric current or equivalent magnetic current can be expanded by the RWG basis function [31], thus, the above equivalent currents can be expressed as

$$\text{PEC region } S_1 \quad \eta_0 \boldsymbol{J}_1 = \sum_{j=1}^{N_1} a_j \boldsymbol{f}_{1j} \tag{1}$$

$$\text{Dielectric region } S_2 \begin{cases} \eta_0 \boldsymbol{J}_2 = \sum_{j=1}^{N_2} b_j \boldsymbol{f}_{2j} \\ \boldsymbol{M}_2 = \sum_{j=1}^{N_2} c_j \boldsymbol{f}_{2j} \end{cases} \tag{2}$$

$$\text{Divisional Environment } S_4 \begin{cases} \eta_0 \boldsymbol{J}_{\mathrm{KA}} = \sum_{j=1}^{N_4} d_j \boldsymbol{f}_{4j} \\ \boldsymbol{M}_{\mathrm{KA}} = \sum_{j=1}^{N_4} e_j \boldsymbol{f}_{4j} \end{cases} \tag{3}$$

where η_0 is wave impedance in free space, which can be written as $\eta_0 = \sqrt{\mu_0/\varepsilon_0}$. a_j, b_j, c_j, d_j and e_j are expansion coefficients. In Ref. [25], the inner surface of dielectric part of combined target is defined as the surface $S_{\mathrm{d}} = S_2 + S_3$, and only effective electric current $\boldsymbol{J}_{2\mathrm{e}}^{\mathrm{eff}}$ will be stimulated on the inner surface S_{d}, which can be expanded by the RWG basis function as follow

$$-\eta_0 \boldsymbol{J}_{2\mathrm{e}}^{\mathrm{eff}} = \sum_{j=1}^{N_2} g_j \boldsymbol{f}_{2j} + \sum_{j=1}^{N_3} h_j \boldsymbol{f}_{3j} \tag{4}$$

where g_j and h_j are expansion coefficients. From the boundary condition of dielectric rough surface, we obtain the following equations that are $\boldsymbol{J}_{\mathrm{KA}} = \hat{\boldsymbol{n}}_4 \times \boldsymbol{H}_{\mathrm{sur}}$ and $\boldsymbol{M}_{\mathrm{KA}} = -\hat{\boldsymbol{n}}_4 \times \boldsymbol{E}_{\mathrm{sur}}$, where $\hat{\boldsymbol{n}}_4$ is the unit normal vector of arbitrary point in coastal environment. $\boldsymbol{E}_{\mathrm{sur}}$ and $\boldsymbol{H}_{\mathrm{sur}}$ denotes total electric field and total magnetic field of coastal environment, respectively. Total electric field $\boldsymbol{E}_{\mathrm{sur}}$ only depends on incident electric field $\boldsymbol{E}^{\mathrm{i}}$ and scattering electric field $\boldsymbol{E}_{\mathrm{sur}}^{\mathrm{s}}$ when no target exists above coastal environment. Correspondingly, total magnetic field $\boldsymbol{H}_{\mathrm{sur}}$ depends on incident magnetic field $\boldsymbol{H}^{\mathrm{i}}$ and scattering magnetic field $\boldsymbol{H}_{\mathrm{sur}}^{\mathrm{s}}$ from pure coastal

environment. When target is reckoned in, the existence of it will become the secondary incidence resource to illuminate the divisional rough surface. Then, the total electric field $\boldsymbol{E}_{\text{sur}}$ and magnetic field $\boldsymbol{H}_{\text{sur}}$ can be expressed as

$$\boldsymbol{E}_{\text{sur}} = \boldsymbol{E}^{\text{i}} + \boldsymbol{E}^{\text{s}}_{\text{sur}} + \boldsymbol{E}^{\text{s}}_{\text{t-sur}} \tag{5}$$
$$\boldsymbol{H}_{\text{sur}} = \boldsymbol{H}^{\text{i}} + \boldsymbol{H}^{\text{s}}_{\text{sur}} + \boldsymbol{H}^{\text{s}}_{\text{t-sur}} \tag{6}$$

where $\boldsymbol{E}^{\text{s}}_{\text{t-sur}}$ and $\boldsymbol{H}^{\text{s}}_{\text{t-sur}}$ present incident electric field and incident magnetic field from the combined target respectively, whose expressions can be written as

$$\boldsymbol{E}^{\text{s}}_{\text{t-sur}} = -\eta_0 \boldsymbol{L}_{01}(\boldsymbol{J}_1) - \eta_0 \boldsymbol{L}_{02}(\boldsymbol{J}_2) + \boldsymbol{K}_{02}(\boldsymbol{M}_2) \tag{7}$$
$$\boldsymbol{H}^{\text{s}}_{\text{t-sur}} = -\boldsymbol{K}_{01}(\boldsymbol{J}_1) - (1/\eta_0)\boldsymbol{L}_{02}(\boldsymbol{M}_2) - \boldsymbol{K}_{02}(\boldsymbol{J}_2) \tag{8}$$

Here, we identify the electric field integral operator (EFIO) and magnetic field integral operator (MFIO) as $\boldsymbol{L}_{0z}(\cdot)$ and $\boldsymbol{K}_{0z}(\cdot)$ respectively, whose expressions are given in the Equation (7) in Ref. [36]. When the relationship between incident wavelength λ and curvature radius ρ of arbitrary point in divisional rough surface meets $\rho \gg \lambda$, the Kirchhoff approximation can be applied. The scattering electric field and magnetic field of divisional rough surface can be expressed as

$$\boldsymbol{E}^{\text{s}}_{\text{sur}} = \Gamma_{\parallel} E^{\text{i}}_{\parallel} \hat{\boldsymbol{e}}_{\text{i}\parallel} + \Gamma_{\perp} E^{\text{i}}_{\perp} \hat{\boldsymbol{e}}_{\text{i}\perp} + \Gamma_{\parallel} E^{\text{s}}_{\text{t-sur}\parallel} \hat{\boldsymbol{e}}_{\text{i}\parallel} + \Gamma_{\perp} E^{\text{s}}_{\text{t-sur}\perp} \hat{\boldsymbol{e}}_{\text{i}\perp} \tag{9}$$

$$\boldsymbol{H}^{\text{s}}_{\text{sur}} = \frac{1}{\eta_0} \hat{\boldsymbol{k}}_{\text{r}} \times (\Gamma_{\parallel} E^{\text{i}}_{\parallel} \hat{\boldsymbol{e}}_{\text{i}\parallel} + \Gamma_{\perp} E^{\text{i}}_{\perp} \hat{\boldsymbol{e}}_{\text{i}\perp} + \Gamma_{\parallel} E^{\text{s}}_{\text{t-sur}\parallel} \hat{\boldsymbol{e}}_{\text{i}\parallel} + \Gamma_{\perp} E^{\text{s}}_{\text{t-sur}\perp} \hat{\boldsymbol{e}}_{\text{i}\perp}) \tag{10}$$

where $\hat{\boldsymbol{k}}_{\text{r}} = \hat{\boldsymbol{k}}_{\text{i}} - 2\hat{\boldsymbol{n}}(\hat{\boldsymbol{n}} \cdot \hat{\boldsymbol{k}}_{\text{i}})$ presents the local reflection direction and $\hat{\boldsymbol{k}}_i$ presents the local incident direction; Set the local orthogonal system is $(\hat{\boldsymbol{e}}_{\text{i}\parallel}, \hat{\boldsymbol{e}}_{\text{i}\perp}, \hat{\boldsymbol{k}}_{\text{i}})$; $\hat{\boldsymbol{e}}_{\text{i}\parallel} = \left(\hat{\boldsymbol{n}} \times \hat{\boldsymbol{k}}_{\text{i}}\right) / \left|\hat{\boldsymbol{n}} \times \hat{\boldsymbol{k}}_{\text{i}}\right|$ and $\hat{\boldsymbol{e}}_{\text{i}\perp} = \hat{\boldsymbol{e}}_{\text{i}\parallel} \times \hat{\boldsymbol{k}}_{\text{i}}$ denote the vector of horizontal polarization and vertical polarization respectively; $\Gamma_{\parallel}$ and $\Gamma_{\perp}$ denote horizontal and vertical polarization component of Fresnel reflection coefficient, whose expressions are given in Equation (9) in Ref. [36], where ε_{r} and μ_{r} denote relative permittivity and relative permeability of local surface; $\theta' = \arccos(-\hat{\boldsymbol{n}} \cdot \hat{\boldsymbol{k}}_i)$ denotes the local incident angle. The incident magnetic field can be written as

$$\boldsymbol{H}^{\text{i}} = (1/\eta_0)\hat{\boldsymbol{k}}_{\text{i}} \times (E^{\text{i}}_{\parallel} \hat{\boldsymbol{e}}_{\text{i}\parallel} + E^{\text{i}}_{\perp} \hat{\boldsymbol{e}}_{\text{i}\perp} + E^{\text{s}}_{\text{t-sur}\parallel} \hat{\boldsymbol{e}}_{\text{i}\parallel} + E^{\text{s}}_{\text{t-sur}\perp} \hat{\boldsymbol{e}}_{\text{i}\perp}) \tag{11}$$

Then, the total electric field $\boldsymbol{E}_{\text{sur}}$ and magnetic field $\boldsymbol{H}_{\text{sur}}$ of divisional rough surface can be obtained with (9), (10) and (11), which can be rewritten as

$$\begin{aligned}\boldsymbol{E}_{\text{sur}} = {} & E^{\text{i}}_{\parallel} \hat{\boldsymbol{e}}_{i\parallel} + E^{\text{i}}_{\perp} \hat{\boldsymbol{e}}_{\text{i}\perp} + E^{\text{s}}_{\text{t-sur}\parallel} \hat{\boldsymbol{e}}_{\text{i}\parallel} + E^{\text{s}}_{\text{t-sur}\perp} \hat{\boldsymbol{e}}_{\text{i}\perp} \\ & + \Gamma_{\parallel} E^{\text{i}}_{\parallel} \hat{\boldsymbol{e}}_{\text{i}\parallel} + \Gamma_{\perp} E^{\text{i}}_{\perp} \hat{\boldsymbol{e}}_{\text{i}\perp} + \Gamma_{\parallel} E^{\text{s}}_{\text{t-sur}\parallel} \hat{\boldsymbol{e}}_{\text{i}\parallel} + \Gamma_{\perp} E^{\text{s}}_{\text{t-sur}\perp} \hat{\boldsymbol{e}}_{\text{i}\perp}\end{aligned} \tag{12}$$

$$\begin{aligned}\boldsymbol{H}_{\text{sur}} = {} & (1/\eta_0)\hat{\boldsymbol{k}}_{\text{i}} \times (E^{\text{i}}_{\parallel} \hat{\boldsymbol{e}}_{i\parallel} + E^{\text{i}}_{\perp} \hat{\boldsymbol{e}}_{\text{i}\perp} + E^{\text{s}}_{\text{t-sur}\parallel} \hat{\boldsymbol{e}}_{\text{i}\parallel} + E^{\text{s}}_{\text{t-sur}\perp} \hat{\boldsymbol{e}}_{\text{i}\perp}) \\ & + (1/\eta_0)\hat{\boldsymbol{k}}_{\text{r}} \times (\Gamma_{\parallel} E^{\text{i}}_{\parallel} \hat{\boldsymbol{e}}_{\text{i}\parallel} + \Gamma_{\perp} E^{\text{i}}_{\perp} \hat{\boldsymbol{e}}_{\text{i}\perp} + \Gamma_{\parallel} E^{\text{s}}_{\text{t-sur}\parallel} \hat{\boldsymbol{e}}_{\text{i}\parallel} \\ & + \Gamma_{\perp} E^{\text{s}}_{\text{t-sur}\perp} \hat{\boldsymbol{e}}_{\text{i}\perp})\end{aligned} \tag{13}$$

From the boundary condition of dielectric rough surface, $\boldsymbol{J}_{\text{KA}}$ and $\boldsymbol{M}_{\text{KA}}$ along the divisional rough surface can be written as

$$\begin{aligned}\boldsymbol{J}_{\text{KA}} = {} & (1/\eta_0)\hat{\boldsymbol{n}}_4 \times \left\{ \hat{\boldsymbol{k}}_{\text{i}} \times \left[(\boldsymbol{E}^{\text{i}} + \boldsymbol{E}^{\text{s}}_{\text{t-sur}}) \cdot \bar{\bar{\boldsymbol{e}}}_{\text{i}\parallel} + (\boldsymbol{E}^{\text{i}} + \boldsymbol{E}^{\text{s}}_{\text{t-sur}}) \cdot \bar{\bar{\boldsymbol{e}}}_{\text{i}\perp} \right] \right. \\ & \left. + \hat{\boldsymbol{k}}_{\text{r}} \times \left[\Gamma_{\parallel} (\boldsymbol{E}^{\text{i}} + \boldsymbol{E}^{\text{s}}_{\text{t-sur}}) \cdot \bar{\bar{\boldsymbol{e}}}_{\text{i}\parallel} + \Gamma_{\perp} (\boldsymbol{E}^{\text{i}} + \boldsymbol{E}^{\text{s}}_{\text{t-sur}}) \cdot \bar{\bar{\boldsymbol{e}}}_{\text{i}\perp} \right] \right\}\end{aligned} \tag{14}$$

$$\begin{aligned}\boldsymbol{M}_{\text{KA}} = {} & -\hat{\boldsymbol{n}}_4 \times \left\{ (1 + \Gamma_{\parallel}) \left[(\boldsymbol{E}^{\text{i}} + \boldsymbol{E}^{\text{s}}_{\text{t-sur}}) \cdot \bar{\bar{\boldsymbol{e}}}_{\text{i}\parallel} \right] \right. \\ & \left. (1 + \Gamma_{\perp}) \left[(\boldsymbol{E}^{\text{i}} + \boldsymbol{E}^{\text{s}}_{\text{t-sur}}) \cdot \bar{\bar{\boldsymbol{e}}}_{\text{i}\perp} \right] \right\}\end{aligned} \tag{15}$$

where $\bar{\bar{\boldsymbol{e}}}_{\text{i}\parallel} = \hat{\boldsymbol{e}}_{\text{i}\parallel}\hat{\boldsymbol{e}}_{\text{i}\parallel}$ and $\bar{\bar{\boldsymbol{e}}}_{\text{i}\perp} = \hat{\boldsymbol{e}}_{\text{i}\perp}\hat{\boldsymbol{e}}_{\text{i}\perp}$ present the dyadic of horizontal and vertical polarization. Substitute (1), (2), (3) and (7), (8) into (14) and (15), then both sides of (14) and (15) are tested by $\hat{\boldsymbol{n}}_4 \times \boldsymbol{f}_{4i}$, the expressions of (14) and (15) can be written in vector matrix form as follow

$$\{d\} = [D_{41}] \cdot \{a\} + [D_{42}] \cdot \{b\} + [F_{42}] \cdot \{c\} + \{W\} \tag{16}$$
$$\{e\} = [E_{41}] \cdot \{a\} + [E_{42}] \cdot \{b\} + [Y_{42}] \cdot \{c\} + \{V\} \tag{17}$$

where expressions of matrix elements in (16) can be found in Equation (14) in Ref. [36], and expressions of matrix elements in (17) are taken in these forms

$$\begin{aligned}E_{4q}(i,j) = {} & \int_{T_{4i}} \boldsymbol{f}_{4i}(\boldsymbol{r}) \cdot \left[(1 + \Gamma_{\parallel}) \boldsymbol{L}_{0q}(\boldsymbol{f}_{qj}) \cdot \bar{\bar{\boldsymbol{e}}}_{\text{i}\parallel} + (1 + \Gamma_{\perp}) \cdot \right. \\ & \left. \boldsymbol{L}_{0q}(\boldsymbol{f}_{qj}) \cdot \bar{\bar{\boldsymbol{e}}}_{\text{i}\perp} \right] dS, i \in [1, N_4], j \in [1, N_q], \quad q = 1, 2.\end{aligned} \tag{18}$$

$$\begin{aligned}Y_{42}(i,j) = {} & -\int_{T_{4i}} \boldsymbol{f}_{4i}(\boldsymbol{r}) \cdot \left[(1 + \Gamma_{\parallel}) \boldsymbol{K}_{02}(\boldsymbol{f}_{2j}) \cdot \bar{\bar{\boldsymbol{e}}}_{\text{i}\parallel} + (1 + \Gamma_{\perp}) \cdot \right. \\ & \left. \boldsymbol{K}_{02}(\boldsymbol{f}_{2j}) \cdot \bar{\bar{\boldsymbol{e}}}_{\text{i}\perp} dS, \quad i \in [1, N_4], \ j \in [1, N_2] \right.\end{aligned} \tag{19}$$

$$\begin{aligned}V(i) = {} & -\int_{T_{4i}} \boldsymbol{f}_{4i}(\boldsymbol{r}) \cdot \left[(1 + \Gamma_{\parallel}) \boldsymbol{E}^{\text{i}}(\boldsymbol{r}) \cdot \bar{\bar{\boldsymbol{e}}}_{\text{i}\parallel} + (1 + \Gamma_{\perp}) \cdot \right. \\ & \left. \boldsymbol{E}^{\text{i}}(\boldsymbol{r}) \cdot \bar{\bar{\boldsymbol{e}}}_{\text{i}\perp} dS, \quad i \in [1, N_4] \right.\end{aligned} \tag{20}$$

The electric field integral equation (EFIE) in S_1 of combined target can be written as

$$\hat{\boldsymbol{n}}_1 \times \boldsymbol{E}^{\text{s}}_{\text{t}} = -\hat{\boldsymbol{n}}_1 \times (\boldsymbol{E}^{\text{i}} + \boldsymbol{E}^{\text{s}}_{\text{sur-t}}), \boldsymbol{r} \in S_1 \tag{21}$$

Correspondingly, the EFIE and magnetic field integral equation (MFIE) in S_2 of combined target can be written as

$$\hat{\boldsymbol{n}}_2 \times \boldsymbol{E}^{\text{s}}_{\text{t}} = -\hat{\boldsymbol{n}}_2 \times (\boldsymbol{E}^{\text{i}} + \boldsymbol{E}^{\text{s}}_{\text{sur-t}}), \quad \boldsymbol{r} \in S_2 \tag{22}$$
$$\hat{\boldsymbol{n}}_2 \times \boldsymbol{H}^{\text{s}}_{\text{t}} = -\hat{\boldsymbol{n}}_2 \times (\boldsymbol{H}^{\text{i}} + \boldsymbol{H}^{\text{s}}_{\text{sur-t}}), \quad \boldsymbol{r} \in S_2 \tag{23}$$

where $\boldsymbol{E}^{\text{s}}_{\text{t}}$ and $\boldsymbol{H}^{\text{s}}_{\text{t}}$ present the scattering electric and magnetic field of combined target, whose expressions are the same as (7) and (8); when incident wave illuminates the surface of coastal environment, the existence of surface will become the secondary incidence resource to illuminate the

combined target. $\boldsymbol{E}^{\mathrm{s}}_{\text{sur-t}}$ and $\boldsymbol{H}^{\mathrm{s}}_{\text{sur-t}}$ present incident electric field and incident magnetic field from the divisional rough surface respectively, whose expressions can be written as

$$\boldsymbol{E}^{\mathrm{s}}_{\text{sur-t}} = -\eta_0 \boldsymbol{L}_{04}(\boldsymbol{J}_{\mathrm{KA}}) + \boldsymbol{K}_{04}(\boldsymbol{M}_{\mathrm{KA}}) \tag{24}$$

$$\boldsymbol{H}^{\mathrm{s}}_{\text{sur-t}} = -(1/\eta_0)\boldsymbol{L}_{04}(\boldsymbol{M}_{\mathrm{KA}}) - \boldsymbol{K}_{04}(\boldsymbol{J}_{\mathrm{KA}}) \tag{25}$$

By substituting (7) and (24) into (22) and (23), we have

$$\begin{aligned}&\hat{\boldsymbol{n}}_1 \times \boldsymbol{E}^{\mathrm{i}} \\ &= \hat{\boldsymbol{n}}_1 \times \Big[\boldsymbol{L}_{01}(\eta_0 \boldsymbol{J}_1) + \boldsymbol{L}_{02}(\eta_0 \boldsymbol{J}_2) - \tilde{\boldsymbol{K}}_{02}(\boldsymbol{M}_2) \\ &\quad + \boldsymbol{L}_{04}(\eta_0 \boldsymbol{J}_{\mathrm{KA}}) - \tilde{\boldsymbol{K}}_{04}(\boldsymbol{M}_{\mathrm{KA}})\Big]\end{aligned} \tag{26}$$

$$\begin{aligned}&\hat{\boldsymbol{n}}_2 \times \boldsymbol{E}^{\mathrm{i}} \\ &= \hat{\boldsymbol{n}}_2 \times [\boldsymbol{L}_{01}(\eta_0 \boldsymbol{J}_1) + \boldsymbol{L}_{02}(\eta_0 \boldsymbol{J}_2) - (1/2)\boldsymbol{M}_2 - \tilde{\boldsymbol{K}}_{02}(\boldsymbol{M}_2) \\ &\quad + \boldsymbol{L}_{04}(\eta_0 \boldsymbol{J}_{\mathrm{KA}}) - (1/2)\boldsymbol{M}_{\mathrm{KA}} - \tilde{\boldsymbol{K}}_{04}(\boldsymbol{M}_{\mathrm{KA}})\Big]\end{aligned} \tag{27}$$

where $\tilde{\boldsymbol{K}}_{02}(\cdot)$ and $\tilde{\boldsymbol{K}}_{04}(\cdot)$ present the principal value integral of $\boldsymbol{K}_{02}(\cdot)$ and $\boldsymbol{K}_{04}(\cdot)$ respectively. Substitute (1), (2), (3) into (26) and (27), both sides of (26) are tested by $\hat{\boldsymbol{n}}_1 \times \boldsymbol{f}_{1i}$, both sides of (27) are tested by $\hat{\boldsymbol{n}}_2 \times \boldsymbol{f}_{2i}$, the expressions of (26) and (27) can be written in vector matrix form as follow

$$\begin{aligned}&[Q_{11}] \cdot \{a\} + [Q_{12}] \cdot \{b\} + [P_{12}] \cdot \{c\} + [R_{14}] \cdot \{d\} \\ &\quad + [T_{14}] \cdot \{e\} = \{S_1\}\end{aligned} \tag{28}$$

$$\begin{aligned}&[Q_{21}] \cdot \{a\} + [Q_{22}] \cdot \{b\} + [P_{22}] \cdot \{c\} + [R_{24}] \cdot \{d\} \\ &\quad + [T_{24}] \cdot \{e\} = \{S_2\}\end{aligned} \tag{29}$$

where expression of matrix element Q_{11}, Q_{12}, Q_{21}, Q_{22}, P_{12}, P_{22}, R_{14} and R_{24} can be found in Equation (20) in Ref. [36]. The matrix element T_{14} and T_{24} are taken into these forms

$$T_{p4}(i,j) = -\int_{T_{pi}} \boldsymbol{f}_{pi}(\boldsymbol{r}) \cdot \tilde{\boldsymbol{K}}_{04}(\boldsymbol{f}_{4j}) dS,\ i \in [1, N_p],\ j \in [1, N_4],\ p = 1, 2. \tag{30}$$

When we substitute (16) and (17) into (28) and (29), only three groups of unknowns remain to be solved: $\{a\}$, $\{b\}$ and $\{c\}$. For solving $\{a\}$, $\{b\}$ and $\{c\}$, the fields within the dielectric part of combined target must to be taken into consideration. In usual coupled integral equation method the electrical field $\boldsymbol{E}_{\mathrm{d}}$ and magnetic field $\boldsymbol{H}_{\mathrm{d}}$ in the interior region ($S_{\mathrm{d}} = S_2 + S_3$) of combined target's dielectric part could be calculated by the pair of equivalent currents $(\boldsymbol{J}_2, \boldsymbol{M}_2)$, but with the opposite sign by

$$\boldsymbol{E}_{\mathrm{d}} = -\eta_1 \boldsymbol{L}_{1\mathrm{d}}(-\boldsymbol{J}_2) + \boldsymbol{K}_{1\mathrm{d}}(-\boldsymbol{M}_2) \tag{31}$$

$$\boldsymbol{H}_{\mathrm{d}} = -(1/\eta_1)\boldsymbol{L}_{1\mathrm{d}}(-\boldsymbol{M}_2) - \boldsymbol{K}_{1\mathrm{d}}(-\boldsymbol{J}_2) \tag{32}$$

Then, utilizing the SIE method, the electric field $\boldsymbol{E}_{\mathrm{d}}$ and magnetic field $\boldsymbol{H}_{\mathrm{d}}$ generated by the effective electric current $\boldsymbol{J}^{\mathrm{eff}}_{2\mathrm{e}}$ [22] along the inner surface S_{d}, whose expressions can be written as

$$\boldsymbol{E}_{\mathrm{d}} = -\eta_1 \boldsymbol{L}_{1\mathrm{d}}(\boldsymbol{J}^{\mathrm{eff}}_{2\mathrm{e}}) \tag{33}$$

$$\boldsymbol{H}_{\mathrm{d}} = -\boldsymbol{K}_{1\mathrm{d}}(\boldsymbol{J}^{\mathrm{eff}}_{2\mathrm{e}}) \tag{34}$$

where η_1 is wave impedance, which can be written as $\eta_1 = \sqrt{\mu_1/\varepsilon_1}$; The operator $\boldsymbol{L}_{1\mathrm{d}}(\cdot)$ and $\boldsymbol{K}_{1\mathrm{d}}(\cdot)$ are the same as the Equation (7) in Ref. [36] by adjusting the corresponding medium parameters in them, and the operation of integral is carried out over the inner surface S_{d}. The fields in the inner surface S_{d} satisfy Maxwell's equations, and the tangential fields are continuous across the surface of dielectric part. From the boundary conditions, we have

$$\boldsymbol{J}_2 = \hat{\boldsymbol{n}}_2 \times \boldsymbol{H}_{\mathrm{d}} = -(1/2)\boldsymbol{J}^{\mathrm{eff}}_{2\mathrm{e}} - \hat{\boldsymbol{n}}_2 \times \tilde{\boldsymbol{K}}_{1\mathrm{d}}(\boldsymbol{J}^{\mathrm{eff}}_{2\mathrm{e}}) \tag{35}$$

$$-\boldsymbol{M}_2 = \hat{\boldsymbol{n}}_2 \times \boldsymbol{E}_{\mathrm{d}} = -\hat{\boldsymbol{n}}_2 \times \eta_1 \boldsymbol{L}_{1\mathrm{d}}(\boldsymbol{J}^{\mathrm{eff}}_{2\mathrm{e}}) \tag{36}$$

where $\tilde{\boldsymbol{K}}_{1\mathrm{d}}(\cdot)$ presents the principal value integral of $\boldsymbol{K}_{1\mathrm{d}}(\cdot)$. The tangential component of electric field on the contacting surface S_3 disappears, thus, we have

$$0 = \hat{\boldsymbol{n}}_3 \times \boldsymbol{E}_{\mathrm{d}} = -\hat{\boldsymbol{n}}_3 \times \eta_1 \boldsymbol{L}_{1\mathrm{d}}(\boldsymbol{J}^{\mathrm{eff}}_{2\mathrm{e}}) \tag{37}$$

Using RWG basis function, the expansion form of $\boldsymbol{J}^{\mathrm{eff}}_{2\mathrm{e}}$ is given in (4), and the expansion coefficient g_j and h_j can be obtained by average value of edge electric current as the same as the Equation (23) in Ref. [36]. Substitute (2) into (35) and (36), then, both sides of (35) and (36) are tested by $\hat{\boldsymbol{n}}_2 \times \boldsymbol{f}_{2i}$, both sides of (37) are tested by $\hat{\boldsymbol{n}}_3 \times \boldsymbol{f}_{3i}$, the expressions of (35)-(37) can be written in vector matrix form as follow

$$\{b\} = [\tilde{M}_{22}] \cdot \{g\} + [\tilde{M}_{23}] \cdot \{h\} \tag{38}$$

$$\{c\} = [\tilde{N}_{22}] \cdot \{g\} + [\tilde{N}_{23}] \cdot \{h\} \tag{39}$$

$$\{0\} = [\tilde{B}_{32}] \cdot \{g\} + [\tilde{B}_{33}] \cdot \{h\} \tag{40}$$

where the expressions of matrix elements can be found in Equation (25) in Ref. [36]. By substituting (38), (39) and (40) into (28) and (29), the matrix equation can be rewritten as

$$\begin{bmatrix} A_{11} & A_{12} & A_{13} \\ A_{21} & A_{22} & A_{23} \\ 0 & A_{32} & A_{33} \end{bmatrix} \cdot \begin{Bmatrix} a \\ g \\ h \end{Bmatrix} = \begin{Bmatrix} \tilde{S}_1 \\ \tilde{S}_2 \\ 0 \end{Bmatrix} \tag{41}$$

where expressions of matrix elements are taken in these forms

$$[A_{11}] = [Q_{11}] + [R_{14}] \cdot [D_{41}] + [T_{14}] \cdot [E_{41}] \tag{42}$$

$$\begin{aligned}[A_{12}] = &([Q_{12}] + [R_{14}] \cdot [D_{42}] + [T_{14}] \cdot [E_{42}]) \cdot \left[\tilde{M}_{22}\right] \\ &+ ([P_{12}] + [R_{14}] \cdot [F_{42}] + [T_{14}] \cdot [Y_{42}]) \cdot \left[\tilde{N}_{22}\right]\end{aligned} \tag{43}$$

$$\begin{aligned}[A_{13}] = &([Q_{12}] + [R_{14}] \cdot [D_{42}] + [T_{14}] \cdot [E_{42}]) \cdot \left[\tilde{M}_{23}\right] \\ &+ ([P_{12}] + [R_{14}] \cdot [F_{42}] + [T_{14}] \cdot [Y_{42}]) \cdot \left[\tilde{N}_{23}\right]\end{aligned} \tag{44}$$

$$[A_{21}] = [Q_{21}] + [R_{24}] \cdot [D_{41}] + [T_{24}] \cdot [E_{41}] \tag{45}$$

$$\begin{aligned}[A_{22}] = &([Q_{22}] + [R_{24}] \cdot [D_{42}] + [T_{24}] \cdot [E_{42}]) \cdot \left[\tilde{M}_{22}\right] \\ &+ ([P_{22}] + [R_{24}] \cdot [F_{42}] + [T_{24}] \cdot [Y_{42}]) \cdot \left[\tilde{N}_{22}\right]\end{aligned} \tag{46}$$

$$\begin{aligned}[A_{23}] = &([Q_{22}] + [R_{24}] \cdot [D_{42}] + [T_{24}] \cdot [E_{42}]) \cdot \left[\tilde{M}_{23}\right] \\ &+ ([P_{22}] + [R_{24}] \cdot [F_{42}] + [T_{24}] \cdot [Y_{42}]) \cdot \left[\tilde{N}_{23}\right]\end{aligned} \tag{47}$$

$$[A_{32}] = \left[\tilde{B}_{32}\right] \tag{48}$$

$$[A_{33}] = \left[\tilde{B}_{33}\right] \tag{49}$$

$$\left[\tilde{S}_1\right] = \{S_1\} - [R_{14}] \cdot \{W\} - [T_{14}] \cdot \{V\} \tag{50}$$

$$\left[\tilde{S}_2\right] = \{S_2\} - [R_{24}] \cdot \{W\} - [T_{24}] \cdot \{V\} \tag{51}$$

B. ACCELERATION OF SIE-KA USING THE MULTILEVEL FAST MULTIPOLE ALGORITHM

In order to improve the efficiency of the aforementioned hybrid method, MLFMA being an effective accelerating technique can be introduced for accelerating the matrix-vector multiplications (MVMs). Initially, when implementing the MLFMA, an Oct-tree structure needs to be generated. In detail: a box enclosing the whole scattering model is named as the zero level, which is divided into eight smaller boxes named the 1st level; then, each box is recursively divided into finer sub-boxes until the edge length of the finest cube D_f is about 0.25λ, and the final level is the total number of levels L_f. The interactions between these boxes can be divided into the near-region couplings and the far-region couplings, which are calculated by the direct MOM and the fast multipole method (FMM) respectively. The essence of FMM is expression of Green function, which is based on the vector addition theorem.

$$\begin{aligned} G(\boldsymbol{r}_o, \boldsymbol{r}_{o'}) &= \frac{e^{-jk|\boldsymbol{r}_o - \boldsymbol{r}_{o'}|}}{4\pi\,|\boldsymbol{r}_o - \boldsymbol{r}_{o'}|} \\ &= \frac{-jk}{(4\pi)^2} \oint d^2\hat{k} e^{-j\boldsymbol{k}\boldsymbol{r}_{om}} T(\hat{k}, \hat{\boldsymbol{r}}_{mm'}) e^{j\boldsymbol{k}\boldsymbol{r}_{o'm'}} \end{aligned} \tag{52}$$

where

$$T(\hat{k}, \boldsymbol{r}_{mm'}) = \sum_{l=0}^{L} (-j)^l (2l+1) h_l^{(2)}(kr_{mm'}) P_l(\hat{k} \cdot \hat{\boldsymbol{r}}_{mm'}) \tag{53}$$

Correspondingly, the dyadic expression of Green function can be written as follow

$$\begin{aligned} \bar{\bar{G}}(\boldsymbol{r}_o, \boldsymbol{r}_{o'}) &= (\bar{\bar{\boldsymbol{I}}} - \frac{\nabla\nabla'}{k}) \frac{e^{-jk|\boldsymbol{r}_o - \boldsymbol{r}_{o'}|}}{4\pi\,|\boldsymbol{r}_o - \boldsymbol{r}_{o'}|} \\ &= \frac{-jk}{(4\pi)^2} \oint d^2\hat{k} (\bar{\bar{\boldsymbol{I}}} - \hat{k}\hat{k}) e^{-j\boldsymbol{k}\boldsymbol{r}_{om}} T(\hat{k}, \boldsymbol{r}_{mm'}) e^{j\boldsymbol{k}\boldsymbol{r}_{o'm'}} \end{aligned} \tag{54}$$

Here, $\boldsymbol{r}_o$ resides in cube m centered at $\boldsymbol{r}_m$, $\boldsymbol{r}_{o'}$ resides in cube m' centered at $\boldsymbol{r}_{m'}$, and their relationships are: $\boldsymbol{r}_{om} = \boldsymbol{r}_o - \boldsymbol{r}_m$, $\boldsymbol{r}_{o'm'} = \boldsymbol{r}_{o'} - \boldsymbol{r}_{m'}$. $h_l^{(2)}(\cdot)$ denotes the spherical Hankel function of the second kind; $P_l(\cdot)$ denotes the Legendre polynomial of degree l; L is the number of multipole expansion terms, and it can ensure high precision when set as $L = kD_f + 5\ln(kD_f + \pi)$. The expressions of matrix elements in matrix (16) and (17): D_{41}, D_{42}, F_{42}, E_{41}, E_{42} and Y_{42} are taken into these forms

$$\begin{aligned} D_{4q}(i,j) = \int\int d^2\hat{k} (&U_{im}^{D_{44}} \cdot T_{mm'}(\boldsymbol{k}_0, \boldsymbol{r}_{mm'}) V_{jm'}^{D_{qq}} \\ &+ M_{im}^{D_{44}} \cdot T_{mm'}(\boldsymbol{k}_0, \boldsymbol{r}_{mm'}) N_{jm'}^{D_{qq}}) \\ &q = 1, 2. \end{aligned} \tag{55}$$

$$\begin{aligned} F_{42}(i,j) = \int\int d^2\hat{k} (&U_{im}^{F_{44}} \cdot T_{mm'}(\boldsymbol{k}_0, \boldsymbol{r}_{mm'}) V_{jm'}^{F_{22}} \\ &+ M_{im}^{F_{44}} \cdot T_{mm'}(\boldsymbol{k}_0, \boldsymbol{r}_{mm'}) N_{jm'}^{F_{22}}) \end{aligned} \tag{56}$$

$$E_{4q}(i,j) = \int\int d^2\hat{k} U_{im}^{E_{44}} \cdot T_{mm'}(\boldsymbol{k}_0, \boldsymbol{r}_{mm'}) V_{jm'}^{E_{qq}}, q = 1, 2. \tag{57}$$

$$Y_{42}(i,j) = \int\int d^2\hat{k} U_{im}^{Y_{44}} \cdot T_{mm'}(\boldsymbol{k}_0, \boldsymbol{r}_{mm'}) V_{jm'}^{Y_{22}} \tag{58}$$

The expressions of each element in (55) to (58) are provided in appendix (1-10). Where $U_{im}^{(\cdot)}/M_{im}^{(\cdot)}$, $T_{mm'}(\cdot)$ and $V_{jm'}^{(\cdot)}/N_{jm'}^{(\cdot)}$ are the disaggregation, translation and aggregation matrices on the concrete level respectively. Apply FMM to the integral equation of target, the matrix elements for far-region groups in matrix (28) and (29) Q_{11}, Q_{12}, Q_{21}, Q_{22}, P_{12}, P_{22}, R_{14}, R_{24}, T_{14} and T_{24} can be written as

$$Q_{pq}(i,j) = \int\int d^2\hat{k} U_{im}^{Q_{pp}} \cdot T_{mm'}(\boldsymbol{k}_0, \boldsymbol{r}_{mm'}) V_{jm'}^{Q_{qq}},\ p, q = 1, 2. \tag{59}$$

$$P_{12}(i,j) = \int\int d^2\hat{k} U_{im}^{P_{11}} \cdot T_{mm'}(\boldsymbol{k}_0, \boldsymbol{r}_{mm'}) V_{jm'}^{P_{22}} \tag{60}$$

$$P_{22}(i,j) = -(\delta_{ij}/2) + \int\int d^2\hat{k} U_{im}^{P_{22}} \cdot T_{mm'}(\boldsymbol{k}_0, \boldsymbol{r}_{mm'}) V_{jm'}^{P_{22}} \tag{61}$$

$$R_{p4}(i,j) = \int\int d^2\hat{k} U_{im}^{R_{pp}} \cdot T_{mm'}(\boldsymbol{k}_0, \boldsymbol{r}_{mm'}) V_{jm'}^{R_{44}}, \quad p = 1, 2. \tag{62}$$

$$T_{p4}(i,j) = \int\int d^2\hat{k} U_{im}^{T_{pp}} \cdot T_{mm'}(\boldsymbol{k}_0, \boldsymbol{r}_{mm'}) V_{jm'}^{T_{44}}, \quad p = 1, 2. \tag{63}$$

The expressions of each element in (59) to (63) are provided in appendix (11-18). Where $U_{im}^{(\cdot)}$, $T_{mm'}(\cdot)$ and $V_{jm'}^{(\cdot)}$ are the disaggregation, translation and aggregation matrices on the concrete level respectively. In terms of Green function in dielectric region, the specific implementation process of FMM has to change according to the electromagnetic parameters of dielectric region particularly. Hence, in SIE method, the matrix elements for far-region groups in matrix (38), (39) and (40) $\tilde{M}_{22}$, $\tilde{M}_{23}$, $\tilde{N}_{22}$, $\tilde{N}_{23}$, $\tilde{B}_{32}$ and $\tilde{B}_{33}$ can be found in Equation (33) in Ref. [36].

Aggregation processes of in above integral equations are implemented by indirectly calculate these matrices elements with interpolation from the (L_f-1)-th level to the second level successively. Translation processes are carried out on each level. Detailed description of the MLFMA can be found in [16], and it will not be repeated here. Based on the above theory and formulations, the hybrid SIE-KA method with MLFMA are formed to calculate EM scattering from three-dimensional arbitrarily shaped combined conducting and dielectric target above coastal environment. We adopt the bi-conjugate gradient method (Bi-CGM) [37] to solve the matrix equation (41) iteratively. When the relative error of unknown electric/magnetic current between the n-th step and (n-1)-th step is less than 10^{-4}, the iterative computation stops.

TABLE 1. Memory requirement and computational complexity.

Method	Number of unknowns	Memory requirement	Computational complexity
Conventional MOM	$N_1+2N_2+N_3+N_4$	$o((N_1+2N_2+N_3+N_4)^2)$	$o((N_1+2N_2+N_3+N_4)^2)$
MLFMA	$N_1+2N_2+N_3+N_4$	$o((N_1+2N_2+N_3+N_4)\log(N_1+2N_2+N_3+N_4))$	$o((N_1+2N_2+N_3+N_4)\log(N_1+2N_2+N_3+N_4))$
SIE	$N_1+N_2+N_3+N_4$	$o((N_1+N_2+N_3+N_4)^2)$	$o((N_1+N_2+N_3+N_4)^2)$
SIE-MLFMA	$N_1+N_2+N_3+N_4$	$o((N_1+N_2+N_3+N_4)\log(N_1+N_2+N_3+N_4))$	$o((N_1+N_2+N_3+N_4)\log(N_1+N_2+N_3+N_4))$
SIE-KA	$N_1+N_2+N_3+N_4$	$o(N_4(N_1+N_2+N_3)^2)$	$o(N_4\,(N_1+N_2+N_3)^2)$
SIE-KA-MLFMA	$N_1+N_2+N_3+N_4$	$o(N_4(N_1+N_2+N_3)\log(N_1+N_2+N_3))$	$o(N_4(N_1+N_2+N_3)\log(N_1+N_2+N_3))$

C. MEMORY REQUIREMENT AND COMPUTATIONAL COMPLEXITY

To validate the efficiency of the hybrid SIE-KA-MLFMA method, the memory requirement and computational complexity are necessarily investigated and compared with some other methods, such as conventional MOM with Bi-CGM (based on coupled integral equation method), the SIE method (target by SIE, rough surface by MOM), the hybrid SIE-MLFMA method, the hybrid SIE-KA method and the hybrid SIE-KA-MLFMA method. The comparison of the memory requirement and computational complexity of different methods is shown in Table 1.

As shown in Table 1, conventional MOM has the most number of unknowns, and other four methods have the same number of unknowns. Comparing conventional MOM and SIE, when introducing SIE, the number of unknowns in dielectric part of combined target is cut off by half, meanwhile, the memory requirement and computational complexity reduce correspondingly. When combining SIE with KA, the original dimension of impendence matrix will be reduced and just depend on the number of target's unknowns $(N_1+N_2+N_3)$, The memory requirement and computational complexity of SIE-KA is $o(N_4(N_1+N_2+N_3)^2)$. In general, the number of environmental unknowns N_4 is much bigger than target's unknowns $(N_1+N_2+N_3)$. However, the good performance of SIE-KA only exists on the premise of this condition that the number of target's unknowns is relatively small. When the number of target's unknowns increases, high memory requirement and high computational complexity are still the major burden of computational process. Through analysis of this table, the SIE-KA is suitable for solving the composite EM scattering problem with larger environmental unknowns and relatively smaller target's unknowns. When combining SIE with MLFMA, the hybrid SIE-MLFMA method has better performance comparing with SIE in both memory requirement and computational complexity. But the SIE-MLFMA still has to endure the enormous number of unknowns which contains both combined target and divisional rough surface. In practical radar detection, the personal computer will not suffice the huge memory requirement with the larger number of actual target's unknowns, and the hybrid SIE-KA-MLFMA method would be more suitable for this application. By applying MLFMA, the SIE-KA-MLFMA has smaller computational complexity and requires less memory. This table shows us three important conclusions: firstly, the SIE is efficient in reducing the number of unknowns; secondly, the introduction of KA allows us to solve a composite EM scattering problem with a large-scale environment; finally, the application of MLFMA makes the composite EM scattering problem with the electrically large targets solvable.

The validation of the hybrid SIE-KA-MLFMA method will be verified by the representative computation examples at the beginning of Section III. Abundant numerical simulations will be further exhibited. Meanwhile, several special phenomena and interesting results will be shown and some important conclusions will be discussed in the section.

III. NUMERICALSIMULATION AND DISCUSSION

A. MODELING OF COASTAL ENVIRONMENT

The surface of ground region is simulated by using Gaussian spectral function, whose statistic properties depend on the RMS $h_{\rm rms}$ and correlation length $l_{\rm x}$, $l_{\rm y}$ (along the x-axis and y-axis direction). When we establish the surface model of sea surface, the concrete location of sea region must be considered. When the waves approach the seashore, the finite depth of this shallow sea region will have effects on the shape and statistic properties of sea surface. Bases on energy flux conservation theorem, shoaling coefficient is introduced by McCormick to connect shoaling effect with sea spectrum [38]. The validation of shoaling coefficient is verified during near sea experiments by Brinkkjar and Jonsson [39]. Therefore, we introduce the finite-depth sea spectrum [40] which combines JONSWAP spectrum and shoaling coefficient to simulate the near sea surface of coastal environment. The shoaling coefficient $\zeta(d)$ is the function of sea depth d and the sea wave number k, which can be written in this form

$$\zeta(d)=\sqrt{\frac{\cosh^2(kd)}{\sinh(kd)\cosh(kd)+kd}} \tag{64}$$

The relationship between the sea frequency and k is given as follow

$$f=\sqrt{g_c k(1+k^2/k_m^2)\tanh(kd)}/2\pi \tag{65}$$

where k_m denotes the wavenumber with minimum phase speed, $k_m = 363.2\text{rad/m}$; $g_{\rm c}$ is gravity acceleration,

$g_c = 9.81 m/s^2$. The finite-depth sea spectrum is taken in this form

$$S_{\text{Finite}}(f, d) = \zeta^2(d) \cdot S_{\text{JONSWAP}}(f) \tag{66}$$

where $S_{\text{JONSWAP}}(f)$ is the JONSWAP spectrum, and its expression [40] is shown as follow

$$S_{\text{JONSWAP}}(f) = \frac{\alpha g_c^2}{(2\pi)^4 f^5} \exp\left[-\frac{5}{4}\left(\frac{f_m}{f}\right)^4\right] \gamma^{\exp\left[-\frac{(f-f_m)^2}{2\sigma_J^2 f_m^2}\right]} \tag{67}$$

where α is dimensionless constant, $\alpha = 0.076(g_c X/v_{10})^{-0.22}$; X denotes wind fetch and v_{10} denotes wind velocity on the height of 10.0 m above sea surface. f_m is the frequency corresponding to spectral peaks, $f_m = 3.5 g_c^{0.67}/(X^{0.33} v_{10}^{0.34})$. γ is enhancement factor of peak value, whose observation value ranges from 1.5 to 6 and mean value is 3.3. σ_J is peak shape parameter which is defined as follow

$$\sigma_J = \begin{cases} 0.07, & f \le f_m \\ 0.09, & f > f_m \end{cases} \tag{68}$$

When we establish the surface of near sea region, the water depth distribution of this region should be considered. Due to the limitation of our group, the measured datum of real near sea's water depth cannot be obtained easily. Analytically, we can build a sketch map of profile for near sea's water depth distribution based on the research report of the East China Sea submarine topography [41]. In the East China Sea, the seafloor of continental shelf is divided into inner continental shelf and outer continental shelf. In the region of outer continental shelf, the slope of seabed is stabilized at approximately 1.0‰, and the water depth is approximately 60 m. But in the region of inner continental shelf (extending from land about 10 km), the slope is ranging from 0 to 0.9 [41]. In this paper, we introduce an approximate way to build the profile model for near sea's water depth distribution, which is given in Figure 2 in Ref. [33]. According to the approximate model in [34], the slope of inner continental shelf is assumed to be 0.7, where H_{near} denotes water depth and L_{shelf} denotes the extended distance of continental shelf. The method is just a simple and approximate way to simulate the water depth distribution in near sea region. If the measured datum of real near sea's water depth is available, the effect of water depth on sea spectrum will be more practical and reasonable.

Based on the suitable sea spectrum for near sea region, we adopt the theory of composite rough surface modeling [33] to establish the geometrical model for coastal environment. In order to deal with the boundary between ground region and near sea region, the weighted inverse tangent function is utilized, whose expression is shown as follow:

$$f_{com}(x, y) = f_{sur1}(x, y) \cdot \frac{[\pi/2 + \arctan f_w(x, y)]}{\pi} + f_{sur2}(x, y) \cdot \frac{[\pi/2 - \arctan f_w(x, y)]}{\pi} \tag{69}$$

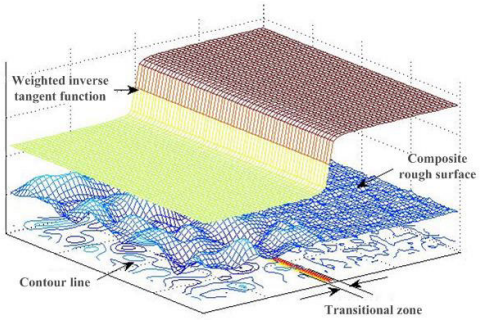

FIGURE 2. The sketch map of composite rough surface after treatment of weighted inverse tangent function.

where $f_{sur1}(x, y)$, $f_{sur2}(x, y)$ and $f_{com}(x, y)$ denote height profiles of rough surface *sur*1, rough surface *sur*2 and composite rough surface *com*, respectively; $f_w(x, y)$ denotes the weighted function for borderline modulation, and its concrete form could be confirmed by the structure of actual environment. The sketch map of composite rough surface after treatment of weighted inverse tangent function is shown as follow:

As shown in Figure 2, the weighted inverse tangent function is a key processing to connect two different regions and smooth the borderline. In this paper, we choose the linear boundary (Equation (9) in Ref. [33]) to build the geometrical model of coastal environment.

The working frequency is set as $f = 300$MHz; Size of coastal environment is $L_x \times L_y : 30\lambda \times 30\lambda$; The root mean square (RMS) is set as $h_{\text{rms}} = 0.5\lambda$ and the correlation length in x-axis and y-axis direction are set as $l_x = l_y = 2.0\lambda$; The wind fetch is set as $X = 50$km and wind velocity on the height of 10.0 m above sea surface is set as $v_{10} = 5.0$m/s. The geometrical model of coastal environment is built as shown in Figure 3, which can marvelously simulate the coastal environment. In this paper, the following numerical examples are calculated based on the assumption that each region of divisional environment is homogeneous medium surface. Thus, the approximated treatment is implemented that the relative permittivity of each region is separately assigned by the borderline.

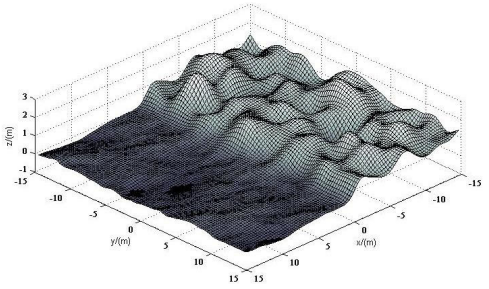

FIGURE 3. The geometrical model of divisional rough surface for coastal environment.

B. VERIFICATION OF HYBRID SIE-KA-MLFMA METHOD

The example of a combined conducting and dielectric sphere above coastal environment is considered in this subsection

to validate the accuracy and to illustrate the efficiency of the hybrid SIE-KA-MLFMA method. In the paper, all computation examples are calculated at the working frequency $f = 1.4$GHz (except for example E). In this subsection and all following subsections (except for example E, F and G), all rough surfaces in computation examples are under the same conditions: Size of coastal environment is $L_x \times L_y$: $30\lambda \times 30\lambda$; The borderline is $x_0 = 0$; The position of each region is shown in Figure 3. In ground region, the RMS is set as $h_{\rm rms} = 0.5\lambda$ and the correlation length in x-axis and y-axis direction are set as $l_x = l_y = 2.0\lambda$; In near sea region, the wind fetch is set as $X = 50$km and wind velocity on the height of 10.0 m above sea surface is set as $v_{10} = 1.0$m/s. The relative permittivity of sea region is set as $\varepsilon_{r-sea} = (72.55, -j63.02)$ when water's salinity s_{water} equals to 32.54‰, temperature is 20°C, which is computed based on the Debye expression proposed in [42]; The relative permittivity of ground region is set as $\varepsilon_{r-gro} = (16.33, -j11.68)$ when sand's content equals to 51.5%, clay's content equals to 13.5%, volumetric water content m_v is 30% and temperature is 20°C, which is computed based on the semi-empirical formulas proposed in [43]. In this paper, incident wave of all computation examples is set as 3-D tapered incident beam, and the tapered parameter $g_{\rm x}$, $g_{\rm y}$ and rough surface length $L_{\rm x}$, $L_{\rm y}$ along x and y axis direction should satisfy $g_{\rm x} = L_{\rm x}/4$ and $g_{\rm y} = L_{\rm y}/4$. As analyzed in the subsection C of Section III, the hybrid SIE-KA method is not suitable for the scattering problems with large target's unknowns. Thus, we choose the MLFMA based on conventional coupled integral equation method as the reference algorithm to compare with the hybrid SIE-KA-MLFMA method in aspects of memory requirement and computation time. The vertical-to-vertical (VV) polarization, vertical-to-horizontal (VH) polarization, horizontal-to-vertical (HV) polarization and horizontal-to- horizontal (HH) polarization are considered. The bi-static RCS of the combined target above divisional rough surface is calculated by MLFMA and SIE-KA-MLFMA respectively. The simulation results are determined by one surface realization. In this paper, the computing platform is AMD processor of 2.3 GHz with 64 kernels and 64 GB RAM. In this computation example, the target is a combined sphere which consists of a PEC hemi-sphere and a dielectric hemi-sphere with permittivity $\varepsilon_{r1} = (4.0, -j2.0)$; Its diameter and height above surface are set as 4.0λ and 5.0λ, respectively. Incident angles are: $\theta_i = 45°$, $\varphi_i = 0°$; Observation angle θ_s is from $-90°$ to $90°$, $\varphi_s = 0°$; The simulation results are shown in Figure 4.

In MLFMA, the number of combined target's unknowns is 43556, and the number of divisional rough surface's unknowns is 274745. By contrast, when introducing SIE, the number of combined target's unknowns reduces to 31495. As analyzed in subsection C of Section II, when applying hybrid SIE-KA method, the dimension of impedance matrix mainly depends on the number of combined target's unknowns instead of the total unknowns, which will bring the great reducing of the memory requirement and improvement of the efficiency. It is observed that the bi-static scattering in

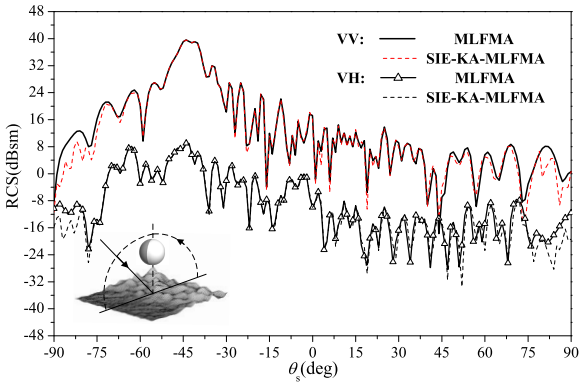

(a) The bi-static RCS curves with VV and VH polarization mode

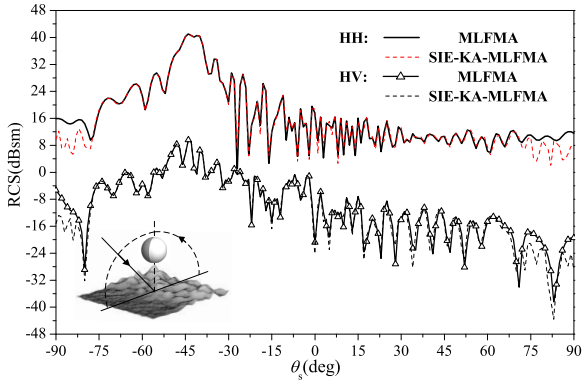

(b) The bi-static RCS curves with HH and HV polarization mode

FIGURE 4. The bi-static RCS curves of a combined sphere above divisional rough surface with MLFMA and SIE-KA-MLFMA.

hybrid SIE-KA-MLFMA method is in good agreement with MLFMA under both co-polarization and cross-polarization. At some large scattering angles, there are some discrepancies existing. These inconsistencies are unsurprising because of the fact that the KA method [29]–[31] has the deficiency in calculating the scattering from rough surface at large scattering angles.

We choose the simulation result with VV polarization in Figure 4 as the example to compare the memory requirement and simulation time of each algorithm listed in Table 1 in detail. The memory requirements of MOM, SIE and SIE-KA are 57.29GB, 51.66GB and 12.18GB, respectively. The simulation time of MOM, SIE and SIE-KA is 9.12 h, 8.32 h and 1.96 h, respectively. Because the multiple surface realizations have to be carried out to solve the composite scattering problems involving rough surfaces, these above algorithms without acceleration strategy are not competent for solving this kind of scattering problem in terms of memory requirement and computing time. Thus, MLFMA should be applied and the detailed comparison of algorithms with the acceleration by MLFMA is given as follow

The memory requirement and simulation time for combined sphere above divisional rough surface with one surface realization by MLFMA, SIE-MLFMA and SIE-KA-MLFMA are presented in Table 2. The memory requirement of

SIE-KA-MLFMA is 23.44% of SIE-MLFMA, 21.14% of MLFMA. The simulation time of SIE-KA-MLFMA is 18.09% of SIE-MLFMA, 16.71% of MLFMA. The table leads us to conclude that the hybrid SIE-KA-MLFMA method is efficient and accuracy for analyzing the 3-D EM scattering from combined conducting and dielectric target above divisional rough surface.

TABLE 2. Memory requirements and simulation times of The MLFMA, SIE-MLFMA and SIE-KA-MLFMA for combined sphere above divisional rough surface with one surface realization.

Solver	Memory Requirement(MB)	Simulation time (s)
MLFMA	713.45	4132.89
SIE-MLFMA	643.34	3817.21
SIE-KA-MLFMA	150.82	690.74

These numerical results lead us to conclude that the hybrid SIE-KA-MLFMA method is efficient in reducing the number of unknowns and memory requirement. It is also a good way to make the composite EM scattering problems of combined target with large divisional rough surface solvable. Based on this hybrid method, plentiful numerical simulations will be exhibited to show the composite EM scattering characteristics of the combined conducting and dielectric target above divisional rough surface in following subsections, and the effect of multifarious factors on the EM scattering characteristics will be discuss in detail.

C. COMPOSITE SCATTERING CHARACTERISTIC WITH DIFFERENT CATEGORY OF ENVIRONMENT

In this example, the composite scattering characteristics of combined cube above single ground rough surface, single sea surface and divisional rough surface are analyzed. The working frequency is set as $f = 1.4$GHz. In this paper, only VV polarization mode is considered, and the polarization characteristics will be studied carefully in example *D*. The side length of combined cube is 5.0λ. The position of combined cube is shown in the sketch map of Figure 5. The target's height above rough surface is 5.0λ. The dielectric part of combined cube is marked by dark color. The dielectric part's permittivity of combined cube is set as $\varepsilon_{r1} = (4.0, -\mathrm{j}2.0)$. The sizes of three rough surfaces are set as $L_x \times L_y : 30\lambda \times 30\lambda$. Each part's statistic parameters of divisional rough surface are the same as that in example *B*. The single ground rough surface's statistic parameters are: $h_{\mathrm{rms}} = 0.5\lambda$, $l_x = l_y = 2.0\lambda$. The single sea surface's statistic parameters are: $X = 50$km, $v_{10} = 1.0$m/s. The relative permittivities of ground region and sea region are set as $\varepsilon_{r-gro} = (16.33, -j11.68)$ and $\varepsilon_{r-sea} = (72.55, -j63.02)$ respectively. Incident angles are: $\theta_i = 45°, \varphi_i = 0°$; Observation angle θ_s is from $-90°$ to $90°$, $\varphi_s = 0°$. Simulation results are shown in Figure 5.

In Figure 5, when the combined cube is located above single sea surface, there is an obvious peak value existing

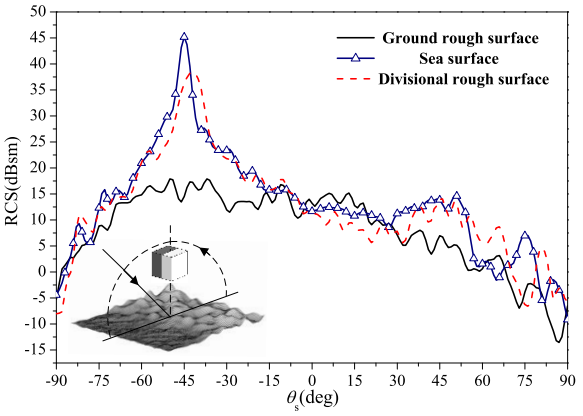

FIGURE 5. Comparison of bi-static RCS curves for a combined cube above single ground rough surface, single sea surface and divisional rough surface.

at the specular scattering direction due to the sea surface's strong specular scattering characteristic. Meanwhile, there is an obvious backscattering in the scattering angle range from 30° to 48°, because quasi-dihedral structure which consists of the relative flat sea surface and the side face of combined cube will bring strong backscattering. However, when the combined cube is located above single ground rough surface, there is no peak value or strong backscattering existing in the bi-static RCS curve due to the ground rough surface's strong diffuse scattering characteristic in all angle range. A valuable discovery is that when the combined cube is located above divisional rough surface, the peak value and the strong backscattering also exist near the direction of specular scattering and backscattering, respectively. But this peak value is smaller than that of single sea surface background, since only the half of divisional rough surface is relatively flat. Due to the existence of ground region, the diffuse scattering in other angles of combined cube above divisional rough surface enhances. The scattering mechanism leading to the strong backscattering is similar to sea surface's condition. The order of backscattering scattering intensity from a combined cube above environment is "single sea surface > divisional rough surface > ground rough surface". According to the comparison of a combined cube above three kinds of rough surface, we can conclude that the combined cube above divisional rough surface presents a unique scattering characteristic which is a fusion of sea surface's specular scattering characteristic and ground rough surface's diffuse scattering characteristic.

D. COMPOSITE SCATTERING CHARACTERISTIC WITH DIFFERENT POLARIZATION MODE

In this example, the composite scattering of a combined cube above divisional rough surface in different polarization mode is analyzed in detail. All concrete parameters of combined cube and divisional rough surface are the same as example *C*. The combined cube is directly above the original point of *xoy* plane, whose height above rough surface is 5.0λ. Incident angles are: $\theta_i = 45°, \varphi_i = 0°$; Observation angle θ_s is from

$-90°$ to $90°$, $\varphi_s = 0°$. The VV polarization, VH polarization, HV polarization and HH are considered. The bi-static RCS curves with different polarization mode are given in Figure 6.

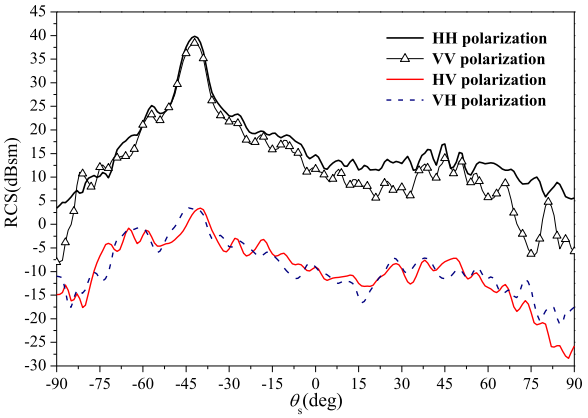

FIGURE 6. The bi-static RCS curves of a combined cube above divisional rough surface with different polarization mode.

As shown in Figure 6, the curve trend of HV polarization is similar to VH polarization, and there are some discrepancies existing between the HH polarization and VV polarization at some scattering angles. The integral values of bi-static RCS curves in co-polarization mode are much larger than that of cross-polarization mode at all scattering angles. Every bi-static RCS curve has a peak region at the specular direction, but the peak value of co-polarization mode is more obvious. Meanwhile, there is an obvious backscattering in the scattering angle range from 33° to 56° in both VV and HH polarization due to the existence of combined cube and relatively flat sea surface. But when polarization mode is HV polarization or VH polarization, the backscattering is not obvious.

E. COMPOSITE SCATTERING CHARACTERISTIC WITH DIFFERENT WORKING FREQUENCY

In this example, the influence of working frequency on the bi-static RCS of a combined cube above divisional rough surface is discussed. The working frequencies are set as: $f_1 =$ 700MHz, $f_2 =$ 1.4GHz and $f_3 =$ 2.1GHz. The combined cube is directly above the original point of *xoy* plane. The side length of combined cube is 0.8 m. The height of combined cube above divisional rough surface is 1.0 m. The size of divisional rough surface is set as $L_x \times L_y$: 6.0m × 6.0m. The statistic parameters of ground region are: $h_{\text{rms}} = 0.1$m, $l_x = l_y = 0.6$m. The statistic parameters of single sea surface's statistic parameters are: $X = 50$km, $v_{10} = 1.0$m/s. Temperature is set as 20°C. Water's salinity equals to 32.54‰. The sea region's relative dielectric constants corresponding to the three frequencies are $\varepsilon'_{r-sea} = (72.88, -\text{j}117.92)$, $\varepsilon''_{r-sea} = (72.55, -\text{j}63.02)$ and $\varepsilon'''_{r-sea} = (72.02, -\text{j}46.47)$. Sand's content equals to 51.5%, clay's content equals to 13.5%, and volumetric water content is 30%. The ground region's relative dielectric constants corresponding to the three frequencies are $\varepsilon'_{r-gro} = (16.38, -\text{j}7.24)$, $\varepsilon''_{r-gro} = (16.33, -\text{j}11.68)$ and $\varepsilon'''_{r-gro} = (16.26, -\text{j}10.28)$. Incident angles are: $\theta_i = 45°$, $\varphi_i = 0°$; Observation angle θ_s is from $-90°$ to $90°$, $\varphi_s = 0°$. The bi-static RCS curves with different working frequency are given in Figure 7.

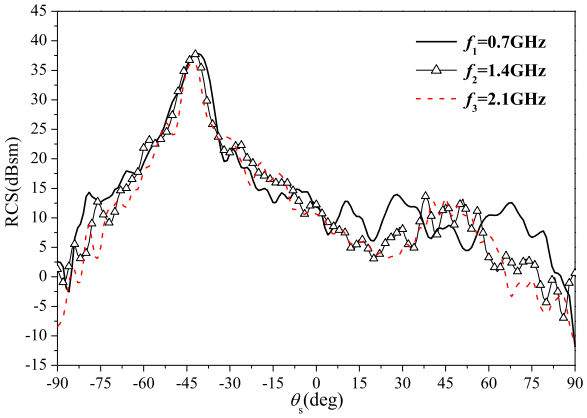

FIGURE 7. The bi-static RCS curves of a combined cube above divisional rough surface with different working frequency.

In Figure 7, with the increase of working frequency, the trend of the bi-static RCS curve keeps stable, however, the scattering energy near the specular scattering direction comes weaker. The backscattering energy also decreases, especially in the scattering angle range from 4° to 37° and from 58° to 90°. Based on the permittivities listed above, we find that working frequency has a little influence on the real part of permittivity but has certain influence on the imaginary part of permittivity. This is one of the reasons causing this phenomenon. The other reason is that when working frequency increases, the divisional rough surface becomes relatively rougher that will enhance the diffuse scattering characteristic of environment. Accordingly, the backscattering will also be effected by the relatively rougher environment.

F. COMPOSITE SCATTERING CHARACTERISTIC WITH DIFFERENT WORKING FREQUENCY

In this example, the influence of ground region's statistic parameters (RMS and correlation length) on the bi-static RCS of a combined cube above divisional rough surface is analyzed in detail. All concrete parameters of combined cube are the same as example *C*. The combined cube is directly above the original point of *xoy* plane, whose height above rough surface is 5.0λ. The wind velocity on the height of 10.0 m above sea surface keeps as $v_{10} = 1.0$m/s. Firstly, we keep the correlation length both in x and y axis direction l_x, l_y stable as 2.0λ. The RMSs are set as $h'_{\text{rms}} = 0.1\lambda$ and $h''_{\text{rms}} = 0.5\lambda$, respectively. Incident angles are: $\theta_i = 45°$, $\varphi_i = 0°$; Observation angle θ_s is from $-90°$ to $90°$, $\varphi_s = 0°$. The bi-static RCS curves with different RMS are given in Figure 8.

With the increase of RMS, the surface of ground part which belongs to the divisional rough surface will become rougher. A slight variation in one part may affect the situation as a whole. In Figure 8, with the increase of RMS, the scattering

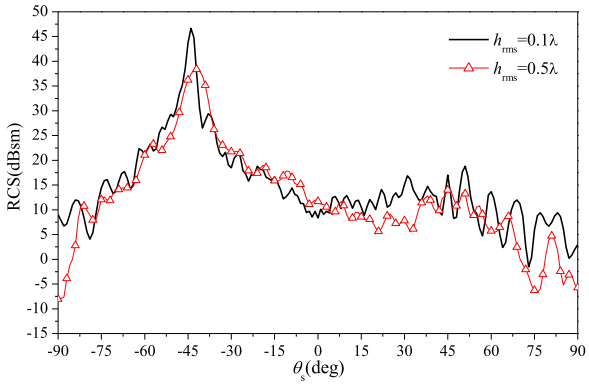

FIGURE 8. The bi-static RCS curves of a combined cube above divisional rough surface with different RMS.

energy near the specular scattering direction decreases significantly, because the rougher ground part enhances the whole environment's diffuse scattering characteristic. In addition, with the increase of RMS, the scattering energy in the range of backscattering also decreases markedly.

Secondly, we take the correlation length of ground region into consideration, because it reflects the correlation between every point on the rough surface which also has effect on surface's roughness. We keep the RMS $h_{\rm rms}$ stable as 0.5λ. The correlation length both in x and y axis direction l_x, l_y are set as $l'_x = l'_y = 2.0\lambda$ and $l''_x = l''_y = 4.0\lambda$, respectively. Incident angles are: $\theta_i = 45°$, $\varphi_i = 0°$; Observation angle θ_s is from $-90°$ to $90°$, $\varphi_s = 0°$. The bi-static RCS curves with different correlation length are given in Figure 9.

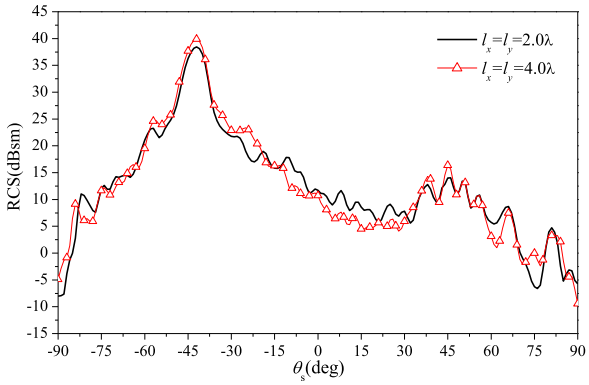

FIGURE 9. The bi-static RCS curves of a combined cube above divisional rough surface with different correlation length.

In Figure 9, with the increase of correlation length, the peak value of bi-static RCS curve increases slightly, and the variation of backscattering is not notable. In the range of scattering angle from -15° to 30°, the value of bi-static RCS curve shows an obvious decline. The reason causes above phenomenon is that with the increase of correlation length, the correlation of every point on the surface of ground part increases, which will make the ground region relatively flatter than before. Therefore, the diffuse scattering characteristic of whole divisional rough surface will be weakened.

G. COMPOSITE SCATTERING CHARACTERISTIC WITH DIFFERENT WIND VELOCITY OF NEAR SEA REGION

In this example, the influence of near sea surface's statistic parameters (wind velocity on the height of 10.0 m above sea surface) on the bi-static RCS of a combined cube above divisional rough surface is discussed. All concrete parameters of combined cube are the same as example C. The combined cube is directly above the original point of xoy plane, whose height above rough surface is 5.0λ. The statistic parameters of ground region keep as: $h_{\rm rms} = 0.5\lambda$ and $l_x = l_y = 2.0\lambda$. The wind velocities on the height of 10.0 m above sea surface are set as: $v'_{10} = 1.0$m/s and $v''_{10} = 5.0$m/s, respectively. Incident angles are: $\theta_i = 45°$, $\varphi_i = 0°$; Observation angle θ_s is from $-90°$ to $90°$, $\varphi_s = 0°$. The bi-static RCS curves with different wind velocity are given in Figure 10.

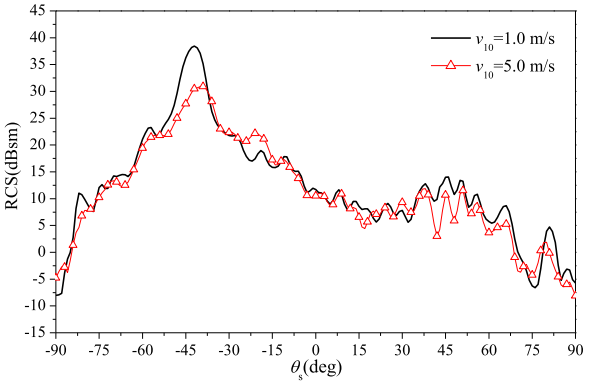

FIGURE 10. The bi-static RCS curves of a combined cube above divisional rough surface with different wind velocity.

With the increase of wind velocity, the surface's fluctuation of near sea part which belongs to the divisional rough surface will become more intense. In Figure 10, with the increase of wind velocity, the scattering energy near the specular scattering direction decreases significantly and the backscattering energy also decreases to some extent. The reason causes above phenomenon is that the whole divisional rough surface's specular scattering characteristic mainly depends on the relatively flat sea surface. Meanwhile, the permittivity of seawater is large. Therefore, the wind velocity also has an obvious effect on the bi-static RCS curve.

H. COMPOSITE SCATTERING CHARACTERISTIC WITH DIFFERENT RELATIVE PERMITTIVITY OF TARGET'S DIELECTRIC PART

In this example, the influence of relative permittivity of target's dielectric part on the bi-static RCS of a combined cube above divisional rough surface is analyzed. All concrete parameters of divisional rough surface are the same as example C. The side length of combined cube is 5.0λ. The combined cube is directly above the original point of xoy plane, whose height above rough surface is 5.0λ. We set two abbreviation Die1 and Die2 to denote the relative permittivity $\varepsilon_{\rm r1} = (4.0, -j2.0)$ and $\varepsilon_{\rm r2} = (8.0, -j4.0)$ respectively.

In Figure 11, we give four combination forms of the combined cube, and the dielectric part is marked by dark color. Incident angles are: $\theta_i = 45°$, $\varphi_i = 0°$; Observation angle θ_s is from $-90°$ to $90°$, $\varphi_s = 0°$. The bi-static RCS curves with different target's combination form are given in Figure 11.

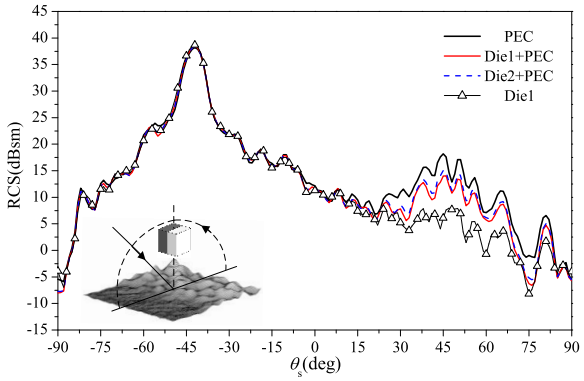

FIGURE 11. The bi-static RCS curves of a combined cube above divisional rough surface with different relative permittivity of target's dielectric part.

In Figure 11, there is an obvious peak value near the specular scattering direction in each curve, but the peak value and its corresponding scattering angle are not varied with the change of the target's combination form because the specular scattering characteristic mainly depends on the properties of divisional rough surface which has been analyzed intensively in previous computation examples. As shown in Figure 11, we can easily find that the target's combination form has a great influence on the backscattering from the combined target above divisional rough surface. When the cube is pure PEC, there is the strongest backscattering near the scattering angle 45°. When the part marked by dark color is replaced by dielectric part with the relative permittivity of Die1, the backscattering decreases remarkably. When the whole cube is replaced by dielectric part with the relative permittivity of Die1, the backscattering is no longer noticeable. These phenomena prove two important conclusions: one is that the dielectric part of an object will reduce its own scattering capability; the other is that the scattering intensity from pure dielectric object is much weaker than that from pure PEC object. What's more, by comparison of the target's combination form "Die1+PEC" and "Die2+PEC", we can find that the backscattering with "Die2+PEC" is stronger than that with "Die1+PEC". Therefore, third important conclusion can be obtained: the dielectric part in combined cube with bigger relative permittivity will lead to stronger backscattering.

I. I. COMPOSITE SCATTERING CHARACTERISTIC WITH DIFFERENT TARGET'S HEIGHT

In this example, the influence of target's height above the divisional rough surface on the bi-static RCS of a combined cube above divisional rough surface is analyzed. All concrete parameters of divisional rough surface are the same as example C. The side length of combined cube is 5.0λ. The combined cube is directly above the original point of xoy plane. The target's heights above the divisional rough surface are set as: $H'_{\text{tar}} = 3.0\lambda$, $H''_{\text{tar}} = 5.0\lambda$ and $H'''_{\text{tar}} = 7.0\lambda$. Incident angles are: $\theta_i = 45°$, $\varphi_i = 0°$; Observation angle θ_s is from $-90°$ to $90°$, $\varphi_s = 0°$. The bi-static RCS curves with different target's height form are given in Figure 12.

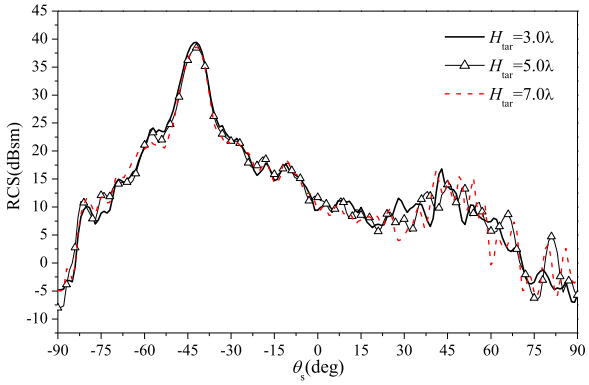

FIGURE 12. The bi-static RCS curves of a combined cube above divisional rough surface with different target's height.

In Figure 12, with the increase of target's height, the value of bi-static RCS curve near the specular scattering direction decreases slightly. The reason causes this phenomenon is that when combined cube is closer to the divisional rough surface, the interaction between target and environment is stronger which will contribute more energy to the specular scattering. In addition, with the increase of target's height, the curve in the backscattering region has no regular variation in intensity or fluctuation, because such an analogous dihedral construction consisting of combined target and divisional rough surface will produce strong backscattering even if the target's height changes within a small range.

J. COMPOSITE SCATTERING CHARACTERISTIC WITH DIFFERENT TARGET'S CATEGORY

The target category and concrete combination form directly determines the scattering characteristics of a combined object. Furthermore, the scattering characteristics of a combined object will affect the composite scattering characteristics. Firstly, we consider a more complicated cube which is divided into four equal-volume parts along the diagonal plane which are vertical to xoy plane. These four parts are marked from "1" to "4" as shown in Figure 13. The geometrical parameters of combined cube and all concrete parameters of divisional rough surface are the same as example C. We set two abbreviation Die1 and Die2 to denote the relative permittivity $\varepsilon_{r1} = (4.0, -j2.0)$ and $\varepsilon_{r2} = (8.0, -j4.0)$ respectively. Incident pitching angle is $\theta_i = 45°$; Observation azimuth angle φ_s is from 0° to 360°, $\theta_s = 45°$. The mono-static RCS curves of different combined cube above divisional rough surface in azimuth angle distribution are given in Figure 13.

As shown in Figure 13, the mono-static scattering energy of a PEC cube above divisional rough surface mainly

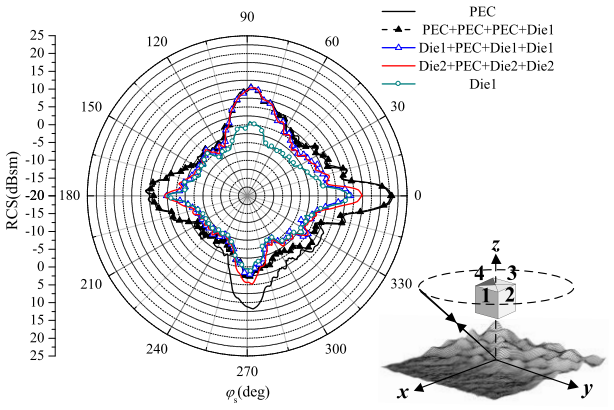

FIGURE 13. The Mono-static RCS curves of different combined cube above divisional rough surface in azimuth angle distribution.

concentrates in four directions, and they are respectively $\varphi_s = 0°$, $\varphi_s = 90°$, $\varphi_s = 180°$ and $\varphi_s = 270°$. Among them, the scattering energy at azimuth angle of 0° is the largest. The scattering energy corresponding to 90° and 270° is at the same level which belongs to the second level. The scattering energy corresponding to 180° is the weakest. The reason causing these four strong peaks is that each side of cube which is vertical to the environment combines with the rough surface as the quasi-dihedral structure which will bring strong backscattering. It is worth mentioning that when azimuth angle is 0°, the side of cube faces the sea surface, when azimuth angle is 90° or 270°, the sides of cube are towards the adjacent region between sea and ground, finally, when azimuth angle is 180°, the side of cube faces ground rough surface. Different environmental surface combined with side of cube will cause different level of backscattering intensity, the order is "sea surface > divisional rough surface > ground rough surface" which is accordance with the conclusion of example *C*. Then, the effect of combination form of cube on the mono-static scattering is analyzed as follow. When the part 4 is replaced by Die1, the scattering intensity has a sharp decline ranging from $\varphi_s = 225°$ to $\varphi_s = 315°$. When the part 1 and part 3 are further replaced by Die1, the sharp decline will occur in the range of 135° to 225°, 0° to 45° and 315° to 360° simultaneously. When all parts are replaced by Die1, the scattering intensity in all azimuth angles decreases dramatically. These three noticeable phenomena prove two important conclusions: one is that the dielectric part of an object will cause a sharp decline in the azimuth angle range where this part is located; the other is that the scattering capability of pure dielectric object is much weaker than that of pure PEC object in whole azimuth distribution. Finally, by comparison of the target's combination form "Die1+PEC+ Die1+Die1" and "Die2+PEC+Die2+Die2", we can find that the scattering intensity of the dielectric part with permittivity Die2 is stronger than that of the dielectric part with permittivity Die1 in corresponding azimuth distribution. Therefore, third important conclusion can be obtained: the dielectric part with bigger permittivity will lead to stronger backscattering in corresponding azimuth distribution. These three conclusions are accordance with the conclusion of example *H*.

Secondly, we consider a complicated cylinder which is divided into four equal-volume parts along the diagonal plane which are vertical to *xoy* plane. These four parts are marked from "1" to "4" as shown in Figure 14. The target's parameters are set as following: diameter of cylinder bottom is 4.0λ, height of cylinder is 4.0λ, and height above surface is 5.0λ respectively. The concrete parameters of divisional rough surface are the same as example *C*. Incident pitching angle is $\theta_i = 45°$; Observation azimuth angle φ_s is from 0° to 360°, $\theta_s = 45°$. The mono-static RCS curves of different combined cylinder above divisional rough surface in azimuth angle distribution are given in Figure 14.

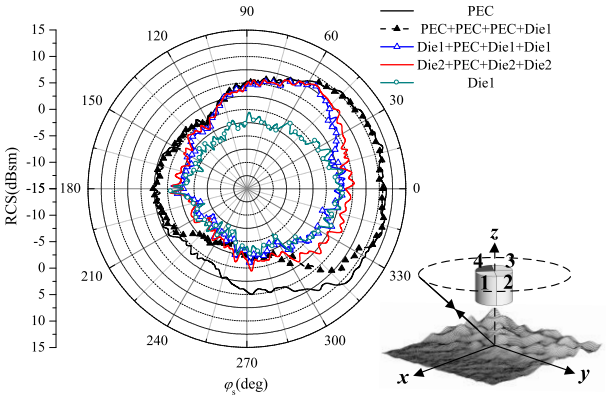

FIGURE 14. The Mono-static RCS curves of different combined cylinder above divisional rough surface in azimuth angle distribution.

Comparing with the results in Figure 14, the distribution of mono-static scattering energy from a PEC cylinder above divisional rough surface in azimuth range is relatively uniform. The reason causes this phenomenon is that the profile of the cylinder is curved surface structure. The peaks which towards $\varphi_s = 0°$, $\varphi_s = 90°$, $\varphi_s = 180°$ and $\varphi_s = 270°$ respectively are not obvious as Figure 13. However, the scattering intensity can still be approximately divided into three levels according to the environmental region which the cylinder's profile faces, the order is "sea surface > divisional rough surface > ground rough surface" which is accordance with the conclusion of example *C* and example *L*. Then, the effect of combination form of cylinder on the mono-static scattering is analyzed as follow. When the part 4 is replaced by Die1, the scattering intensity has a sharp decline ranging from $\varphi_s = 210°$ to $\varphi_s = 330°$, simultaneously. When the part 1 and part 3 are further replaced by Die1, the sharp decline will occur in the range of 0° to 60° and 120° to 360°. If the combination form "Die1+ PEC+Die1+Die1" is varied into "Die2+PEC+Die2+Die2", the mono-static scattering from combined cylinder above divisional rough surface will increase in the range of 0° to 60° and 120° to 360°. When all parts are replaced by Die1, the scattering intensity in all

azimuth angles decreases dramatically. These four noticeable phenomena can also prove the three conclusions in the last example. And the results also verify that they are not the unique phenomena existing in combined cube which contains plane structure, the combined cylinder containing curved surface structure also has the same rules.

K. A COMPOSITE MISSILE MODEL ABOVE DIVISIONAL ROUGH SURFACE

In this example, a composite missile model is considered in order to analyze the composite scattering from it above divisional rough surface. The geometrical parameters of the composite missile model are shown in Figure 15. The concrete parameters of divisional rough surface are the same as example C. The working frequency is set as $f = 1.4$GHz. The composite missile is located above the divisional rough surface with the height of 5.0λ, and its head is toward the positive direction of x-axis. As shown in Figure 15, the nose marked with dark color represents dielectric part with permittivity $\varepsilon_r = (4.0, -j2.0)$ which is expressed as abbreviation Die1. Incident pitching angle θ_i is from $-90°$ to $90°$, and incident azimuth angle φ_s is $0°$. The mono-static RCS curves of the missile model above divisional rough surface are given in Figure 16.

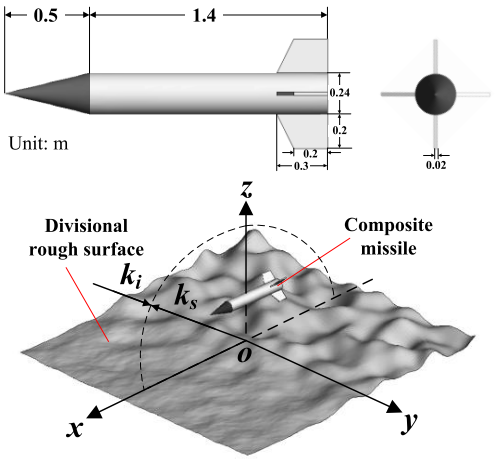

FIGURE 15. Geometrical parameters of the missile model and the configuration of composite missile above divisional rough surface.

As shown in Figure 16, the legend "PEC+Sur" denotes the mono-static RCS curve of PEC missile above divisional rough surface; the legend "Com+Sur" denotes the mono-static RCS curve of composite missile above divisional rough surface; the legend "Sur" denotes the mono-static RCS curve of divisional rough surface; the legend "PEC" and "Com" denote the mono-static RCS curve of PEC missile and composite missile, respectively.

In Figure 16, in the curve of mono-static RCS of divisional rough surface, we can easily find that there is an obvious peak value at the scattering angle of $0°$ in spite of the existence of ground region. In general, if the environment is pure ground rough surface, the large roughness will lead to a strong energy distribution region near the scattering angle of $0°$, rather than a peak value. The unique scattering characteristic of divisional rough surface has been analyzed in detail in example C, and this kind of environment has an important influence on the total field. As we seen, the curves of "PEC+Sur" and "Com+Sur" are similar to the curve of divisional rough surface, and there are just a few discrepancies existing among them at some scattering angles. The effect of the nose's material changing on the total field is not obvious. Thus, a further comparison has to be made to show the effect of dielectric part on the target's scattering characteristics.

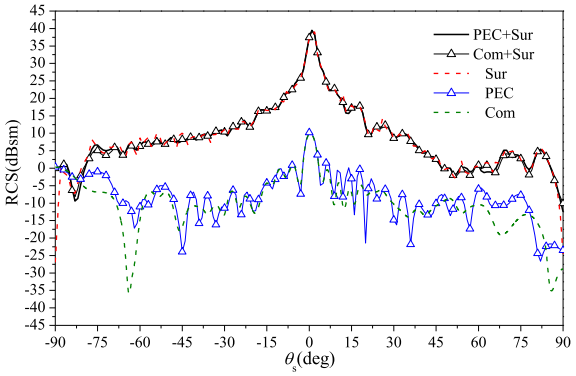

FIGURE 16. The Mono-static RCS curves of missile model above divisional rough surface.

In Figure 16, the material of missile's nose will affect the scattering characteristic of the whole target. When the PEC nose is replaced by the Die1, the scattering intensity from the head-on direction (when $\theta_s = 90°$) has a sharp decline about 5.216dB. The distribution of scattering intensity varies greatly except for the angle range from $-30°$ to $4°$. There are two obvious changes in the angle range: one is from $-90°$ to $-60°$, and the other is $58°$ to $77°$. These phenomena demonstrate the conclusion that the dielectric material is beneficial to the stealth performance of missile in the head-on direction.

IV. CONCLUSION

In this paper, the electromagnetic scattering characteristics of combined target above coastal environment are studied. Due to the multiple media parameters and large amount of unknowns in this composite scattering problem, the hybrid SIE-KA-MLFMA method is proposed. The analysis for the memory requirement and computational complexity of proposed method is discussed in detail, which illustrates the superiority of this hybrid method theoretically. Then, corresponding numerical simulation demonstrates that the proposed algorithm is accurate and efficient. The difference of EM scattering from combined conducting and dielectric target above ground rough surface, sea surface and divisional rough surface are compared. The results of composite scattering show a unique phenomenon which is a fusion of sea surface's specular scattering characteristic and ground rough surface's diffuse scattering characteristic. Moreover, the influences of polarization mode, working frequency,

RMS and correlation length of ground region, wind velocity of near sea region, relative permittivity of target's dielectric part, target's height and target category on composite EM scattering characteristic are discussed in detail. These phenomena prove several important conclusions: first, specular scattering characteristic mainly depends on the properties of coastal environment; second, the dielectric part of an object will reduce its own scattering capability whether in azimuth or pitching range; third, the scattering intensity from pure dielectric object is much weaker than that from pure PEC object; finally, the dielectric part in combined object with bigger relative permittivity will lead to stronger backscattering.

Hence, the proposed hybrid SIE-KA-MLFMA method could be applied as an efficient solver which is suitable for calculating the EM scattering of combined conducting and dielectric object above the coastal environment. In addition, the new laws and characteristics found in these computation examples will have important guidance significance and application value in the field of radar target detection, remote sensing, even stealth technology etc. The main limitations of the proposed method are follows: firstly, it is lack of capability to solve the EM scattering problems of combined target with multi-layered environment; secondly, the uniform dissection rule of the whole scattering model still leads to a large number of environmental unknowns. In order to further reduce the environmental unknowns, the domain decomposition method would be introduced to the improvements of the hybrid method in our future researches. The further works of our research group will focus on the scattering problems about multiple combined target with layered environment or divisional environment with inhomogeneous medium surface, which will simulate more complex situations to explore their inherent laws. The related applications in the field of remote sensing will be studied, and the concrete technologies like radar imaging and target recognition will be further developed in our future works.

APPENDIX

$$U_{im}^{D_{44}} = M_{im}^{D_{44}} = -(k_0^2/16\pi^2)\int_{\Gamma_{4i}} e^{-jk_0\hat{\boldsymbol{k}}\cdot\boldsymbol{r}_{im}}(\bar{\bar{\boldsymbol{I}}} - \hat{k}\hat{k})f_{4i}\times\hat{\boldsymbol{k}}_i dS \quad (70)$$

$$V_{jm'}^{D_{qq}} = \int_{\Gamma_{qj}} e^{jk_0\hat{\boldsymbol{k}}\cdot\boldsymbol{r}_{jm'}}(f_{qj}(\boldsymbol{r}_{jm'})\cdot\hat{\boldsymbol{e}}_{i\parallel}\hat{\boldsymbol{e}}_{i\parallel} + f_{qj}(\boldsymbol{r}_{jm'})\cdot\hat{\boldsymbol{e}}_{i\perp}\hat{\boldsymbol{e}}_{i\perp})dS', \quad q = 1, 2. \quad (71)$$

$$N_{jm'}^{D_{qq}} = \int_{\Gamma_{qj}} e^{jk_0\hat{\boldsymbol{k}}\cdot\boldsymbol{r}_{jm'}}(\Gamma_{\parallel}f_{qj}(\boldsymbol{r}_{jm'})\cdot\hat{\boldsymbol{e}}_{i\parallel}\hat{\boldsymbol{e}}_{i\parallel} + \Gamma_{\perp}f_{qj}(\boldsymbol{r}_{jm'})\cdot\hat{\boldsymbol{e}}_{i\perp}\hat{\boldsymbol{e}}_{i\perp})dS', \quad q = 1, 2. \quad (72)$$

$$U_{im}^{F_{44}} = M_{im}^{F_{44}} = -(k_0^2/16\pi^2)\int_{\Gamma_{4i}} e^{-jk_0\hat{\boldsymbol{k}}\cdot\boldsymbol{r}_{im}} f_{4i}\times\hat{\boldsymbol{k}}_i dS \quad (73)$$

$$V_{jm'}^{F_{22}} = \int_{\Gamma_{2j}} e^{jk_0\hat{\boldsymbol{k}}\cdot\boldsymbol{r}_{jm'}}(f_{2j}(\boldsymbol{r}_{jm'})\times\hat{\boldsymbol{k}}\cdot\hat{\boldsymbol{e}}_{i\parallel}\hat{\boldsymbol{e}}_{i\parallel} + f_{2j}(\boldsymbol{r}_{jm'})\times\hat{\boldsymbol{k}}\cdot\hat{\boldsymbol{e}}_{i\perp}\hat{\boldsymbol{e}}_{i\perp})dS' \quad (74)$$

$$N_{jm'}^{F_{22}} = \int_{\Gamma_{2j}} e^{jk_0\hat{\boldsymbol{k}}\cdot\boldsymbol{r}_{jm'}}(\Gamma_{\parallel}f_{2j}(\boldsymbol{r}_{jm'})\times\hat{\boldsymbol{k}}\cdot\hat{\boldsymbol{e}}_{i\parallel}\hat{\boldsymbol{e}}_{i\parallel} + \Gamma_{\perp}f_{2j}(\boldsymbol{r}_{jm'})\times\hat{\boldsymbol{k}}\cdot\hat{\boldsymbol{e}}_{i\perp}\hat{\boldsymbol{e}}_{i\perp})dS' \quad (75)$$

$$U_{im}^{E_{44}} = (k_0^2/16\pi^2)\int_{\Gamma_{4i}} e^{-jk_0\hat{\boldsymbol{k}}\cdot\boldsymbol{r}_{im}}(\bar{\bar{\boldsymbol{I}}} - \hat{k}\hat{k})f_{4i}(\boldsymbol{r}_{im})dS \quad (76)$$

$$V_{jm'}^{E_{qq}} = \int_{\Gamma_{qj}} e^{jk_0\hat{\boldsymbol{k}}\cdot\boldsymbol{r}_{jm'}}\left[(1+\Gamma_{\parallel})f_{qj}(\boldsymbol{r}_{jm'})\cdot\hat{\boldsymbol{e}}_{i\parallel}\hat{\boldsymbol{e}}_{i\parallel} + (1+\Gamma_{\perp})\cdot f_{qj}(\boldsymbol{r}_{jm'})\cdot\hat{\boldsymbol{e}}_{i\perp}\hat{\boldsymbol{e}}_{i\perp}\right]dS', \quad q = 1, 2. \quad (77)$$

$$U_{im}^{Y_{44}} = (k_0^2/16\pi^2)\int_{\Gamma_{4i}} e^{-jk_0\hat{\boldsymbol{k}}\cdot\boldsymbol{r}_{im}} f_{4i}(\boldsymbol{r}_{im})dS \quad (78)$$

$$V_{jm'}^{Y_{22}} = \int_{\Gamma_{2j}} e^{jk_0\hat{\boldsymbol{k}}\cdot\boldsymbol{r}_{jm'}}\left[(1+\Gamma_{\parallel})f_{2j}(\boldsymbol{r}_{jm'})\times\hat{\boldsymbol{k}}\cdot\hat{\boldsymbol{e}}_{i\parallel}\hat{\boldsymbol{e}}_{i\parallel} + (1+\Gamma_{\perp})\cdot f_{2j}(\boldsymbol{r}_{jm'})\times\hat{\boldsymbol{k}}\cdot\hat{\boldsymbol{e}}_{i\perp}\hat{\boldsymbol{e}}_{i\perp}\right]dS' \quad (79)$$

$$U_{im}^{Q_{pp}} = (k_0^2/16\pi^2)\int_{\Gamma_{pi}} e^{-jk_0\hat{\boldsymbol{k}}\cdot\boldsymbol{r}_{im}} f_{pi}(\boldsymbol{r}_{im})\cdot(\bar{\bar{\boldsymbol{I}}} - \hat{k}\hat{k})dS, \quad p = 1, 2. \quad (80)$$

$$V_{jm'}^{Q_{qq}} = \int_{\Gamma_{qj}} e^{jk_0\hat{\boldsymbol{k}}\cdot\boldsymbol{r}_{jm'}} f_{qj}(\boldsymbol{r}_{jm'})dS', \; q = 1, 2. \quad (81)$$

$$U_{im}^{P_{pp}} = (k_0^2/16\pi^2)\int_{\Gamma_{pi}} e^{-jk_0\hat{\boldsymbol{k}}\cdot\boldsymbol{r}_{im}}(\hat{\boldsymbol{k}}\times f_{pi})dS, p = 1, 2. \quad (82)$$

$$V_{jm'}^{P_{22}} = \int_{\Gamma_{2j}} e^{jk_0\hat{\boldsymbol{k}}\cdot\boldsymbol{r}_{jm'}} f_{2j}(\boldsymbol{r}_{jm'})dS' \quad (83)$$

$$U_{im}^{R_{pp}} = (k_0^2/16\pi^2)\int_{\Gamma_{pi}} e^{-jk_0\hat{\boldsymbol{k}}\cdot\boldsymbol{r}_{im}} f_{pi}(\boldsymbol{r}_{im})\cdot(\bar{\bar{\boldsymbol{I}}} - \hat{k}\hat{k})dS, \quad p = 1, 2. \quad (84)$$

$$V_{jm'}^{R_{44}} = \int_{\Gamma_{4j}} e^{jk_0\hat{\boldsymbol{k}}\cdot\boldsymbol{r}_{jm'}} f_{4j}(\boldsymbol{r}_{jm'})dS' \quad (85)$$

$$U_{im}^{T_{pp}} = (k_0^2/16\pi^2)\int_{\Gamma_{pi}} e^{-jk_0\hat{\boldsymbol{k}}\cdot\boldsymbol{r}_{im}}(\hat{\boldsymbol{k}}\times f_{pi})dS, p = 1, 2. \quad (86)$$

$$V_{jm'}^{T_{44}} = \int_{\Gamma_{4j}} e^{jk_0\hat{\boldsymbol{k}}\cdot\boldsymbol{r}_{jm'}} f_{4j}(\boldsymbol{r}_{jm'})dS' \quad (87)$$

REFERENCES

[1] N. M. Estakhri, B. Edwards, and N. Engheta, "Inverse-designed metastructures that solve equations," *Science*, vol. 363, no. 6433, pp. 1333–1338, Mar. 2019.

[2] N. J. Greybush, V. Pacheco-Peña, N. Engheta, C. B. Murray, and C. R. Kagan, "Plasmonic optical and chiroptical response of self-assembled au nanorod equilateral trimers," *ACS Nano*, vol. 13, pp. 1617–1624, Jan. 2019.

[3] L. La Spada, C. Spooner, S. Haq, and Y. Hao, "Curvilinear MetaSurfaces for surface wave manipulation," *Sci. Rep.*, vol. 9, no. 1, pp. 3107–3117, Dec. 2019.

[4] I.-H. Lee, D. Yoo, P. Avouris, T. Low, and S.-H. Oh, "Graphene acoustic plasmon resonator for ultrasensitive infrared spectroscopy," *Nature Nanotechnol.*, vol. 14, no. 4, pp. 313–319, Apr. 2019.

[5] M. B. Jamshidi, A. Lalbakhsh, J. Talla, Z. Peroutka, F. Hadjilooei, P. Lalbakhsh, M. Jamshidi, L. L. Spada, M. Mirmozafari, M. Dehghani, A. Sabet, S. Roshani, S. Roshani, N. Bayat-Makou, B. Mohamadzade, Z. Malek, A. Jamshidi, S. Kiani, H. Hashemi-Dezaki, and W. Mohyuddin, "Artificial intelligence and COVID-19: Deep learning approaches for diagnosis and treatment," *IEEE Access*, vol. 8, pp. 109581–109595, 2020.

[6] G. Zilman, A. Zapolski, and M. Marom, "On detectability of a ship's Kelvin wake in simulated SAR images of rough sea surface," *IEEE Trans. Geosci. Remote Sens.*, vol. 53, no. 2, pp. 609–619, Feb. 2015.

[7] J. X. Li, M. Zhang, Y. Zhao, and W. Q. Jiang, "Efficient numerical full-polarized facet-based model for EM scattering from rough sea surface within a wide frequency range," *Remote Sens.*, vol. 11, pp. 75–93, Jan. 2019.
[8] X. Duan and M. Moghaddam, "3-D vector electromagnetic scattering from arbitrary random rough surfaces using stabilized extended boundary condition method for remote sensing of soil moisture," *IEEE Trans. Geosci. Remote Sens.*, vol. 50, no. 1, pp. 87–103, Jan. 2012.
[9] P. B. Wei, M. Zhang, D. Nie, and Y. C. Jiao, "Improvement of SSA approach for numerical simulation of sea surface scattering at high microwave bands," *Remote Sens.*, vol. 10, no. 7, pp. 1021–1035, 2018.
[10] A. Tabatabaeenejad and M. Moghaddam, "Study of validity region of small perturbation method for two-layer rough surfaces," *IEEE Geosci. Remote Sens. Lett.*, vol. 7, no. 2, pp. 319–323, Apr. 2010.
[11] J. T. Johnson, "A study of ocean-like surface thermal emission and reflection using Voronovich's small slope approximation," *IEEE Trans. Geosci. Remote Sens.*, vol. 43, no. 2, pp. 306–314, Feb. 2005.
[12] P. Paul and J. P. Webb, "Reducing computational costs using a multi-region finite element method for electromagnetic scattering," *IET Microw., Antennas Propag.*, vol. 2, no. 5, pp. 427–433, Aug. 2008.
[13] S. Rao, D. Wilton, and A. Glisson, "Electromagnetic scattering by surfaces of arbitrary shape," *IEEE Trans. Antennas Propag.*, vol. 30, no. 3, pp. 409–418, May 1982.
[14] R. J. Burkholder and T. Lundin, "Forward-backward iterative physical optics algorithm for computing the RCS of open-ended cavities," *IEEE Trans. Antennas Propag.*, vol. 53, no. 2, pp. 793–799, Feb. 2005.
[15] R. F. Harrington, *Field Computation By Moment Methods*. New York, NY, USA: Macmillan, 1968.
[16] J. M. Song and W. C. Chew, "Multilevel fast-multipole algorithm for solving combined field integral equations of electromagnetic scattering," *Microw. Opt. Technol. Lett.*, vol. 10, no. 1, pp. 14–19, Sep. 1995.
[17] L. Tsang, C. H. Chan, K. Pak, and H. Sangani, "Monte-Carlo simulations of large-scale problems of random rough surface scattering and applications to grazing incidence with the BMIA/canonical grid method," *IEEE Trans. Antennas Propag.*, vol. 43, no. 8, pp. 851–859, 1995.
[18] M. Y. Xia, C. H. Chan, S. Q. Li, B. Zhang, and L. Tsang, "An efficient algorithm for electromagnetic scattering from rough surfaces using a single integral equation and multilevel sparse-matrix canonical-grid method," *IEEE Trans. Antennas Propag.*, vol. 51, no. 6, pp. 1142–1149, Jun. 2003.
[19] Y. Liang, L.-X. Guo, and Z.-S. Wu, "The fast EPILE combined with FBM for electromagnetic scattering from dielectric targets above and below the dielectric rough surface," *IEEE Trans. Geosci. Remote Sens.*, vol. 49, no. 10, pp. 3892–3905, Oct. 2011.
[20] Z. Peng, X.-C. Wang, and J.-F. Lee, "Integral equation based domain decomposition method for solving electromagnetic wave scattering from non-penetrable objects," *IEEE Trans. Antennas Propag.*, vol. 59, no. 9, pp. 3328–3338, Sep. 2011.
[21] M. Jiang, J. Hu, M. Tian, R. Zhao, X. Wei, and Z. Nie, "Solving scattering by multilayer dielectric objects using JMCFIE-DDM-MLFMA," *IEEE Antennas Wireless Propag. Lett.*, vol. 13, pp. 1132–1135, 2014.
[22] M. S. Yeung, "Single integral equation for electromagnetic scattering by three-dimensional homogeneous dielectric objects," *IEEE Trans. Antennas Propag.*, vol. 47, no. 10, pp. 1615–1622, Oct. 1999.
[23] J. M. Taboada, M. G. Araujo, F. O. Basteiro, J. L. Rodriguez, and L. Landesa, "MLFMA-FFT parallel algorithm for the solution of extremely large problems in electromagnetics," *Prog. Electromagn. Res.*, vol. 101, no. 2, pp. 15–30, 2013.
[24] K. Xu, D. Z. Ding, Z. H. Fan, and R. S. Chen, "Multilevel fast multipole algorithm enhanced by GPU parallel technique for electromagnetic scattering problems," *Microw. Opt. Technol. Lett.*, vol. 52, no. 3, pp. 2957–2960, 2010.
[25] W. Fuscaldo, A. Di Simone, L. M. Millefiori, A. Iodice, P. Braca, and P. K. Willett, "A convenient analytical framework for electromagnetic scattering from composite targets," *Radio Sci.*, vol. 54, no. 8, pp. 785–807, Aug. 2019.
[26] Y. Xu, H. Yang, W. Yu, X. Liu, and R. Shen, "Scattering analysis of nonperiodic composite metallic and dielectric structures using synthetic functions," *IEEE Antennas Wireless Propag. Lett.*, vol. 16, pp. 3079–3083, 2017.
[27] G. S. Cheng, D. Z. Ding, and R. S. Chen, "Analysis of transient electromagnetic scattering from composite conducting-dielectric targets with the time-domain fast dipole method," *IEEE Trans. Antennas Propag.*, vol. 65, no. 7, pp. 3800–3805, Jul. 2017.
[28] X. Li, L. Lei, Y. Chen, M. Jiang, P.-H. Jia, Z. Rong, Z. Nie, and J. Hu, "Solving EM scattering from complex thin dielectric/PEC composite targets by a VSIE-based method," *IEEE Trans. Antennas Propag.*, vol. 68, no. 5, pp. 3900–3910, May 2020.
[29] S. Y. He and G. Q. Zhu, "A hybrid MM-PO method combining UV technique for scattering from two-dimensional target above a rough surface," *Microw. Opt. Technol. Lett.*, vol. 49, no. 12, pp. 2957–2960, Dec. 2007.
[30] H. X. Ye and Y. Q. Jin, "A hybrid KA-MOM algorithm for computation of scattering from 3-D PEC target above a dielectric rough surface," *Radio Sci.*, vol. 43, no. 3, pp. 1–15, 2008.
[31] R. Wang, G. Li-Xin, M. Jun, and W. Zhen-Sen, "Hybrid method for investigation of electromagnetic scattering from conducting target above the randomly rough surface," *Chin. Phys. B*, vol. 18, no. 4, pp. 1503–1511, 2009.
[32] H. L. Sun, C. M. Tong, and G. X. Zou, "High efficiency iterative solver for modeling composite rough surface electromagnetic scattering," *Electromagnetics*, vol. 37, no. 2, pp. 113–126, Feb. 2017.
[33] G. X. Zou, C. Ming Tong, H. Long Sun, T. Wang, and P. Peng, "A hybrid method for electromagnetic scattering from target above composite rough surface of ground and near sea in adjacent region," *Electromagnetics*, vol. 38, no. 7, pp. 415–437, Oct. 2018.
[34] G. X. Zou, C. M. Tong, H. L. Sun, T. Wang, and G. L. Tian, "Modeling and electromagnetic scattering of composite rough surface of island in deep sea," in *Proc. Int. Appl. Comput. Electromagn. Soc. Symp.*, 2017, pp. 1–2.
[35] G. Zou, C. Tong, Y. Huang, H. Sun, and T. Wang, "Modeling and electromagnetic scattering of ground and near sea in adjacent region with fractal borderline," in *Proc. 7th Int. Workshop Comput. Sci. Eng.*, 2017, pp. 1055–1060.
[36] G. Zou, C. Tong, H. Sun, P. Peng, and T. Song, "Analysis of electromagnetic scattering from combined conducting and dielectric objects above rough surface using hybrid SIE-KA-FMM method," *IEEE Access*, vol. 7, pp. 95094–95107, 2019.
[37] J. Yi-Zun Wang, R. Ananth, and P. A. Tatem, "Numerical simulation of solid combustion with a robust conjugate gradient solution for pressure," Nav. Res. Lab., Washington, DC, USA, Tech. Rep. 0704-0188, Jul. 2002, pp. 10–13.
[38] M. E. Mccormick, *Ocean Engineering Wave Mechanics*. New York, NY, USA: Wiley, 1973.
[39] O. Brinkkjar and I. G. Jonsson, "Verification of cnoidal shoaling: Putnam and Chinn's experiments," Inst. Hydrodyn. Hydraulic Eng., Tech. Univ. Denmark, Lyngby, Denmark, Prog. Rep. 28, 1973, pp. 19–23.
[40] D. Nie, M. Zhang, C. Wang, and H.-C. Yin, "Study of microwave backscattering from two-dimensional nonlinear surfaces of finite-depth seas," *IEEE Trans. Geosci. Remote Sens.*, vol. 50, no. 11, pp. 4349–4357, Nov. 2012.
[41] Z. C. Liu, Y. L. Chen, J. S. Ding, W. H. Zhang, Y. T. Wu, and F. B. Guo, "Study on zoned characteristics and formation cause of the east China sea submarine topography," *Adv. Mar. Sci.*, vol. 21, no. 2, pp. 160–173, 2003.
[42] L. Klein and C. Swift, "Microwave dielectric behavior of wet soil—Part 1: Empirical models and experimental observations," *IEEE Trans. Antennas Propag.*, vol. 25, no. 1, pp. 104–111, 1977.
[43] M. Hallikainen, F. Ulaby, M. Dobson, M. El-Rayes, and L.-K. Wu, "Microwave dielectric behavior of wet soil—Part 1: Empirical models and experimental observations," *IEEE Trans. Geosci. Remote Sens.*, vol. GE-23, no. 1, pp. 25–34, Jan. 1985.

GAO XIANG ZOU was born in Hunan, China, in 1993. He received the B.S. degree in radar engineering and the M.S. degree in electronics science and technology from Air Force Engineering University, Xi'an, China, in 2015 and 2018, where he is currently pursuing the Ph.D. degree in electromagnetic theory and engineering.

His research interests include computational electromagnetism, Brewster effect, multipath effect, modeling theory of divisional environments, and electromagnetic scattering characteristics of composite targets above divisional environments.

CHUANGMING TONG was born in Hubei, China, in 1964. He received the M.S. and Ph.D. degrees in electromagnetic field and microwave technology from the Air Force Missile College, in 1988 and 1999, respectively.

From 1999 to 2002, he was a Visiting Scholar with the State Key Laboratory of Millimeter Waves, Southeast University, Nanjing, China. He is currently a Professor and a Ph.D. Supervisor with the Air and Missile Defense College, Air Force Engineering University. He is also the Chief Scientist of National 973 project. His research interests include microwave remote sensing, computational electromagnetism, polarimetric and interferometric applications of microwave data, and numerical modeling, ground penetrating radar, through wall imaging, and stealth technology. He has received various fellowships and awards from national and international bodies.

HUA LONG SUN was born in Shaanxi, China, in 1982. He received the B.S. degree in information engineering from the Nanjing University of Aeronautics and Astronautics, Nanjing, China, in 2004, the M.S. degree in electromagnetic field and microwave technology from Southeast University, Nanjing, in 2007, and the Ph.D. degree in electromagnetic theory and engineering from the Air and Missile Defense College, Air Force Engineering University, Xi'an, China, in 2017, where he is currently pursuing the Ph.D. degree in electronics science and technology with the Air and Missile Defense College.

His research interests include multipath effect, radar signal processing, fast electromagnetic calculation method, and electromagnetic scattering characteristics of complex targets and complicated circumstances.

PENG PENG was born in Jiangxi, China, in 1990. He received the B.S. degree in radar engineering and the M.S. degree in electromagnetic field and microwave technology from Air force Engineering University, in 2011 and 2013, respectively. He is currently pursuing the Ph.D. degree with the School of Physics and Optoelectronic Engineering, Xidian University, Xi'an, China.

From 2014 to 2015, he took the Initial Officer Training Course (IOTC) with the Royal Air force College Cranwell, U.K. His research interests include fast algorithms for computational electromagnetics, radar scattering characteristics of the complex target and environment surface, and radar imaging.